An ancient reservoir of volatiles in the Moon sampled by lunar meteorite Northwest Africa 10989

Available online at www.sciencedirect.com

ScienceDirect

Geochimica et Cosmochimica Acta 266 (2019) 163–183

Geochimica et Cosmochimica Acta

www.elsevier.com/locate/gca

An ancient reservoir of volatiles in the Moon sampled by lunar meteorite Northwest Africa 10989

A. Stephant [a,*], M. Anand [a,b], H.O. Ashcroft [a], X. Zhao [a], S. Hu [c], R.L. Korotev [d], S. Strekopytov [e,1], R.C. Greenwood [a], E. Humphreys-Williams [e], Y. Liu [f], G. Tang [f], Q. Li [f], I.A. Franchi [a]

[a] School of Physical Sciences, The Open University, Milton Keynes, UK
[b] Department of Earth Sciences, The Natural History Museum, London, UK
[c] Key Laboratory of Earth and Planetary Physics, Institute of Geology and Geophysics, CAS, Beijing, China
[d] Department of Earth & Planetary Sciences and McDonnell Center for the Space Sciences, Washington University, Saint Louis, MO 63130, United States
[e] Imaging and Analysis Centre, The Natural History Museum, London, UK
[f] State Key Laboratory of Lithospheric Evolution, Institute of Geology and Geophysics, CAS, Beijing, China

Received 29 May 2018; accepted in revised form 24 July 2019; available online 7 August 2019

Abstract

Northwest Africa (NWA) 10989 is a recently found lunar meteorite we used to elucidate the history of volatiles (H and Cl) in the Moon through analysis of its phosphates. The petrology, bulk geochemistry and mineralogy of NWA 10989 are consistent with it being a lunar meteorite with intermediate-iron bulk composition, composed of 40% of mare basaltic material and ~60% non-mare material, but with no obvious KREEP-rich basaltic components. It is probable that the source region for this meteorite resides near a mare–highlands boundary, possibly on the farside of the Moon. Analyses of chlorine and hydrogen abundances and isotopic composition in apatite and merrillite grains from NWA 10989 indicate sampling of at least two distinct reservoirs of volatiles, one being similar to those for known mare basalts from the Apollo collections, while the other potentially represents a yet unrecognized reservoir. In situ Th-U-Pb dating of phosphates reveal two distinct age clusters with one ranging from 3.98 ± 0.04 to 4.20 ± 0.02 Ga, similar to the ages of cryptomare material, and the other ranging from 3.32 ± 0.01 to 3.96 ± 0.03 Ga, closer to the ages of mare basalts known from the Apollo collections. This lunar breccia features mixing of material, among which a basaltic D-poor volatile reservoir which doesn't appear to have been recorded by Apollo samples.

Keywords: Moon; Meteorite; Volatiles

1. INTRODUCTION

The majority of lunar meteorites are thought to originate from areas on the Moon not sampled by the Apollo and Luna missions (Warren and Kallemeyn, 1991; Korotev, 2005), thereby providing a broader coverage across the Moon's surface of both the nearside and the farside. Therefore, lunar meteorites expand our knowledge of the surface composition of the Moon, and enhance our understanding of the bulk composition of the Moon and its evolution throughout its geological history. Brecciated meteorites contain a variety of clast types and geochemical information, providing a snapshot into the material mixing

* Corresponding author.
E-mail address: alice.stephant@open.ac.uk (A. Stephant).
[1] Current address: Inorganic Analysis, National Measurement Laboratory, LGC Ldt, Teddington TW11 0LY, UK.

https://doi.org/10.1016/j.gca.2019.07.045
0016-7037/

processes at the Moon's surface, which occur at local to regional scales, and into the diversity of material that is present at a single location. In terms of their bulk composition, lunar meteorites have been divided into three categories: basaltic (17–23% FeO, 8–12% Al_2O_3), feldspathic (low FeO < 7%, Al_2O_3 > 25%), and intermediate, which contain both basaltic and feldspathic components (Korotev et al., 2009). The intermediate meteorite group has bulk FeO contents between 7 and 17 wt.%, and Al_2O_3 contents between 13 and 20 wt.%, and constitute roughly 25% of the lunar meteorites that exist currently in the worldwide collections (Korotev et al., 2009). These lunar meteorites with intermediate-iron bulk composition could help to understand the crustal evolution on the Moon and are thought either to originate from the boundary between the lunar highlands and mare regions, most likely from the lunar nearside, or to have sampled cryptomare material. The discovery and categorization of more lunar meteorites, particularly meteorites with intermediate-iron bulk composition, suggests that the canonical 'Apollo' model of the Moon, in which all rocks are explained as a mixture of Feldspathic Highland Terrane (FHT), Procellarum KREEP Terrane (PKT), where KREEP stands for potassium (K), rare earth elements (REE), and phosphorous (P) (Warren and Wasson, 1979), and Mare (Jolliff et al., 2000), may not be applicable to the entire lunar surface (Korotev et al., 2009).

In order to identify reservoirs of lunar materials that formed a breccia and possibly locate its source region(s), hydrogen and chlorine isotopic compositions in apatite grains can be useful proxies. As such, mare basalts, KREEP-rich basalts and Mg and Alkali suite materials from Apollo samples appear to have distinct δD-δ^{37}Cl systematics (Sharp et al., 2010; Greenwood et al., 2011; Barnes et al., 2013, 2014, 2016, 2019; Tartèse et al., 2013; Robinson et al., 2016). Nevertheless, analyses of volatiles in new lunar meteorites continue to expand the dataset and to broaden our knowledge of the history of lunar volatiles.

North West Africa (NWA) 10989 is a lunar meteorite that was found near the Morocco–Algeria border in 2014 (Bouvier et al., 2017). This meteorite is a single roughly spherical stone with a dark brown fusion crust that has a diameter of ~2 cm and a mass of 14.41 g. Based on an initial petrographic and geochemical investigation, Ashcroft et al. (2017) classified this meteorite as a mixed lunar fragmental breccia that has intermediate bulk iron content. It is composed of mare- and highlands-derived materials in roughly equal proportions. This study presents a comprehensive mineralogical and geochemical data on mineral, lithic and impact-melt clasts in this meteorite including its bulk-rock major- and trace-element composition, abundance and isotopic composition of chlorine and hydrogen, and U-Th-Pb dates in apatites and a merrillite. This new dataset is then utilized to perform comparisons with other lunar samples in order to gain insights into lunar petrogenetic processes and evaluate potential mantle source region(s) for lithologies contained in NWA 10989.

2. MATERIALS AND ANALYTICAL METHODS

2.1. Petrography

A polished thin section (~1.2 cm × 1.2 cm) of NWA 10989 was prepared at the Open University (OU) for study by optical and scanning electron microscopy (SEM) methods. Microscopic observations under transmitted and reflected light were used to determine the main mineral phases and study the textures of the breccia. Backscattered electron (BSE) and secondary electron (SE) images were collected using the FEI Quanta 3-D FIB-SEM at the OU using beam conditions of 20 kV and 0.6 nA. Qualitative energy-dispersive spectroscopic (EDS) analysis were used for rapid identification of mineral phases. Whole sample and smaller area BSE maps were used as a guide for detailed electron-probe and ion-probe work. In addition, elemental X-ray maps of Al, Ca, Cl, Cr, Fe, Mg, Mn, Na, Ni, K, P, S, Si and Ti were also collected in EDS mode using an Oxford Instruments 80 mm X-MAX energy-dispersive X-ray detector attached to the SEM. A 20 kV accelerating voltage and a 0.60 nA beam current were used during the elemental mapping, and X-ray maps were acquired at 512 × 448 pixels and a magnification of ~300, with a dwell time of 100 µs. The X-ray maps were used to calculate modal mineral abundances in different lithologies/clasts using the ImageJ software.

2.2. Mineral chemistry

Quantitative phase analyses were conducted using a CAMECA SX-100 electron-probe micro-analyzer (EMPA) in wavelength-dispersive spectroscopy (WDS) mode at the OU. An accelerating voltage of 20 kV and a 20 nA beam current were used for silicate, oxide and mineral phases, whereas a 10 nA beam was used for plagioclase and glass analysis to minimize any migration or loss of volatiles. In apatite, F was analysed separately with a 5 µm spot size and a beam at 10 kV and 4 nA, and then the remaining elements were analysed with a 20 kV, 20 nA beam current and 5 µm spot size, using the protocol described by Barnes et al. (2014). Spot sizes of 1, 5 or 10 µm were used depending on crystal size. Counting times were typically 15–40 s on the peak, with background measurements made before and afterwards for half the counting time. Primary standards used for calibration were a range of natural crystals including feldspar (Al, Si, K), jadeite (Na), forsterite (Mg), hematite (Fe), bustamite (Ca, Mn), apatite (P), chromite (Cr), rutile (Ti) and barite (Ba, S) as well as nickel metal (Ni). Secondary pyroxene, olivine, feldspar and apatite standards were run at the start, middle and end of analytical sessions to check the calibration and ensure internal consistency (see Supplementary Table S1).

2.3. Oxygen isotopes

Oxygen isotope analysis was performed at the OU, using an infrared laser-assisted fluorination system (Miller et al., 1999; Greenwood et al., 2017). Oxygen was released from

the samples (one analysis of two aliquots – approximate weight of ~2 mg) by heating in the presence of BrF_5. The released oxygen gas was purified by passing it through two cryogenic nitrogen traps and over a bed of heated KBr. Oxygen gas was analysed using a MAT 253 dual inlet mass spectrometer. Recent levels of precision obtained on the OU system, as demonstrated by 38 analyses of an in-house obsidian standard, were as follows: ±0.053‰ for $\delta^{17}O$; ±0.095‰ for $\delta^{18}O$; ±0.018‰ for $\Delta^{17}O$ (2 SD) (Starkey et al., 2016). Oxygen isotope analyses are reported in standard delta notation. The $\delta^{18}O$ value is calculated as $\delta^{18}O = [(^{18}O/^{16}O)_{sample}/(^{18}O/^{16}O)_{ref} - 1] \times 1000$ (‰). The $\delta^{17}O$ value is calculated as $\delta^{17}O = [(^{17}O/^{16}O)_{sample}/(^{17}O/^{16}O)_{ref} - 1] \times 1000$ (‰). The reference for both is Vienna Standard Mean Ocean Water, VSMOW. The deviation from the terrestrial fractionation line, has been calculated using the linearized format of Miller et al. (2002): $\Delta^{17}O = 1000 \times \ln(1 + \delta^{17}O/1000) - \lambda 1000 \ln(1 + \delta^{18}O/1000)$ where λ is 0.5247. The sample was not pre-treated with ethanolamine thioglycolate (EATG) solution (to remove terrestrial weathering products) and therefore the bulk-rock that was measured for O isotopes would have included some terrestrial material (mainly as fracture-filling veins as seen in optical microscopy).

2.4. Bulk chemistry

The bulk-rock concentrations of major and minor elements (except K_2O) were determined using inductively coupled plasma optical emission spectrometry (ICP-OES; Thermo iCap 6500 Duo) and concentrations of trace elements and potassium were determined using inductively coupled plasma mass spectrometry (ICP-MS; Agilent 7700x) at the Natural History Museum, London. A 40 mg sub-split of homogenized sample powder was used for the ICP-OES analysis and a separate 54.8 mg sub-split was used for the ICP-MS analysis. Analytical details of the both types of analyses are similar to those described in detail by Calzada-Diaz et al. (2017). Quality control was performed by simultaneous analyses of certified reference materials (CRMs), see Supplementary Table S2.

In addition, selected elements were analysed in the bulk-rock by instrumental neutron activation analysis (INAA) at Washington University, St Louis, following the procedure of Korotev et al. (2006). Subsamples were sealed into tubes of ultrapure fused silica (Heraeus-Amersil Suprasil® T21, 5-mm outside diameter). The principal standards for lithophile elements were chips of two synthetic glasses, designated WU-A and WU-B, that were prepared and standardized against the National Bureau of Standards SRM (Standard Reference Material) 1633a, coal flyash (Korotev, 1987). Each batch contained a sample of SRM 1633a powder that was used as the standard for Sc, Sm, and Ta and a cross-check for the glass standards. Finally, each batch contained 2–3 samples of a synthetic chemical standard for Ir and Au. Three subsamples of ~30 mg (32.97, 29.11, 29.11 mg) were analysed. The calculated mass-weighted means, as well as the standard deviation of the three subsamples, are the concentrations that would have been obtained if we had analysed one sample consisting of the entire mass (91.19 mg).

2.5. Chlorine abundance and isotopic measurements

Chlorine abundance and isotopic composition were measured using the Cameca NanoSIMS 50L at the OU using a protocol modified after Tartèse et al. (2014) and Barnes et al. (2016). Analyses were carried out using a Cs^+ primary beam with a diameter of ~1 μm and an accelerating voltage of ~16 kV. Each area was pre-sputtered before analysis for a few minutes using a 150 pA probe current over a 7 μm × 7 μm area to remove any contamination from the surface. Analyses were performed using a primary probe current of 30 pA for ~5 minutes over ~5 μm × 5 μm areas. Secondary negative ions of $^{16}O^1H$, ^{18}O, ^{35}Cl, ^{37}Cl, ^{19}F and $^{40}Ca^{19}F$ were collected simultaneously on electron multipliers. Apatite and merrillite were identified with $^{40}Ca^{19}F$ on real-time secondary ion images during pre-sputtering and to monitor F contents, but was not used for precise quantification of apatite F content, as $^{40}Ca^{19}F$ has poor ionization efficiency. In order to resolve isobaric interferences a mass-resolving power of ~8000 was used, especially for the ^{17}O and $^{16}O^1H$ peaks. Samples were coated with ~20 nm of carbon. Phosphate Cl contents were calibrated using the measured $^{35}Cl/^{18}O$ ratios and the known Cl contents of terrestrial apatite standards Atlas Mountain (Ap 004) and Colorado apatite (Ap 005) (McCubbin et al., 2010, 2012) which were set in an indium mount. Data obtained for standards are provided in Supplementary Table S3. Uncertainties reported on Cl contents combine the expanded uncertainty (coverage factor k = 2) associated with the calibrations and the analytical uncertainties associated with each individual measurement.

2.6. Hydrogen abundance and isotopic measurements

Hydrogen isotopes (D/H) and H_2O abundances were also measured using the Cameca NanoSIMS 50L at the OU. H, D and ^{18}O secondary negative ions were quantified using a Cs+ primary beam of ~530 pA. ^{13}C was also collected simultaneously to monitor possible terrestrial contamination. The primary beam was rastered over a 10 μm × 10 μm and blanking was used to collect signal from only the 5 μm × 5 μm central area during a total analysis duration of ~20 min. Prior to the analysis, the surface was pre-sputtered for 5 minutes using the same beam intensity on a 12 μm × 12 μm surface area. A H^-/O^- vs. H_2O calibration is used to calibrate H_2O concentrations for apatites, based on Durango apatite (Ap 003) and Atlas Mountain apatite (Ap 004) (McCubbin et al., 2010, 2012). Background was monitored using 'dry' olivine San Carlos, and analyses were corrected accordingly. To avoid H contamination, analyses were performed with an analytical chamber vacuum of 4.5×10^{-10} Torr. The background for H_2O was estimated to be 10 ppm, based on constant monitoring analyses of dry San Carlos olivine. For hydrogen isotopic measurements, the instrumental mass fractionation factor α, calculated on standard apatites is 1.23 ± 0.05 (n = 19, 2SD). Because the two standards have

water contents corresponding to the lower and upper ranges of NWA 10989 apatites, and have a restricted range of instrumental mass fractionation, no matrix effects are expected as a function of apatite water contents. Data obtained for standards analysed are presented in Supplementary Table S4.

2.7. Uranium-Thorium-Lead analyses of phosphates

Uranium-Thorium-Lead (U-Th-Pb) dating of six apatites and one merrillite was carried out using the Cameca IMS 1280 at the Institute of Geology and Geophysics, Chinese Academy of Sciences (IGGCAS). The O_2^- primary ion beam was accelerated at −13.8 kV with a current of ~10–12nA. The Gaussian illumination mode was used in order to evenly sputter material over the analytical area. The spot diameter was ~10 μm × 15 μm. Positive secondary ions were extracted with a 10 kV potential. Four magnetic field sequences were used to collect secondary ions $^{40}Ca_2^{31}P^{16}O_3^+$, $^{204}Pb+$, $^{206}Pb^+$, $^{207}Pb^+$, $^{238}U^+$, $^{232}Th^{16}O^+$, $^{238}U^{16}O^+$ and $^{238}U^{16}O_2^+$ (Li et al., 2012). The $^{40}Ca_2^{31}P^{16}O_3^+$ peak was used as a reference peak for centering the secondary ion beam as well as for making energy and mass adjustments. NW-1 apatite standard (1160 ± 5 Ma) was used for U-Pb fractionation calibration (Li et al., 2012) and ages were calculated using Isoplot (Ludwig, 2012). Further technical details can be found in Li et al. (2012) and Zhou et al. (2013). Uranium decay constants for U-Pb geochronology were taken from Schoene et al. (2006).

3. RESULTS

3.1. Petrography

NWA 10989 is a fragmental polymict breccia composed of minerals and mineral fragments, various lithic and impact-melt clasts, embedded in a dark-brown glassy matrix (Fig. 1). The mineral components constituting this breccia include feldspar, olivine (forsteritic as well as fayalitic), pyroxene (opx, low-Ca and high-Ca), and trace amounts of silica, ilmenite, troilite, apatite, merrilite, chromite, schreibersite and kamacite. Despite the meteorite being a find, the terrestrial weathering is limited to minor carbonate veining along cracks and fractures. Evidence for shock recrystallization, where present, can be observed as replacement of millimetre-sized feldspar clasts by submillimetre feldspar crystals. Based on texture and mineral abundances, the polished section of the meteorite was broadly divided into four areas corresponding to distinct lithologies (referred in the text as Areas 1, 2, 3 and 4). Higher magnification BSE images of these four areas are shown in Fig. 1(1c–1f). Among these four areas, a range of clast types set in a fine-grained matrix have been identified, and these can be divided into two categories – lithic fragments and impact-melt clasts, highlighted in Fig. 1. Back-scattered electron images of notable lithic clasts and impact melt clasts, are presented in Figures S1 and S2, respectively, in order to highlight the range of lithologies present. Lithic and impact-melt clasts are further subdivided into different groups based on their texture and composition. Lithic clasts consist of anorthositic troctolite, gabbroic anorthosite, mafic to ultramafic cumulate, granulite and evolved basaltic clasts, based on their relative modal abundances of olivine, pyroxene and plagioclase (Figure S1a), revealing a dominantly feldspathic components. It should be noted that because of the relatively small sizes of these clasts, the observed lithological classification may not truly reflect the parent lithologies from which the clasts were derived (Warren, 2012). Detailed petrography and compositional data of each clast are provided in supplementary information. The representative mineral EMPA compositional data from different clasts are presented in Table S5. The EMPA data for each lithic clast can be found in Supplementary Tables S6 to S9. Impact melt clasts represent both highlands and mare-derived materials. Details on impact melts and matrix glasses are provided in supplementary information, and EMPA data for these are presented in Supplementary Tables S10-S12. Within the studied polished section, we estimate that mafic and feldspathic (non-mare) materials are represented in a ratio of ~40:60, characteristic of a lunar fragmental breccia with intermediate-iron bulk composition. Area 1 (~9% area of the polished section) is a glassy area of impact melt, poorly crystallized in some places, containing large but rare vesicles and mineral fragments, some of which are partly resorbed (Fig. 1c). Area 2 is a crystal-dominated breccia with a cataclastic, seriate texture, with minerals and mineral fragments ranging from ~1 to 100 s μm in size. Impact melt and lithic fragments up to 1 mm in size are rare (Fig. 1d). Area 3 (~64% of the polished section) is a melt-supported breccia containing almost all impact-melt clasts (~8% of the whole section), lithic clasts (~7% of the whole section) and minerals, up to 1 mm in size (Fig. 1e). There is one large (2 mm × 4 mm) clast of a crystallized impact-melt. The surrounding melt is dark brown in colour – when viewed under plane polarized light (PPL) – and contains mineral fragments and vesicles. Area 4 contains mineral fragments similar to Area 2, however, there is a higher proportion of matrix, and some lithic clasts are also present (Fig. 1f). Areas 2 and 4 account for 27% of the whole section. The boundaries between Areas 2, 3 and 4 are gradational.

The lunar meteorite NWA 10989 shows textural similarities to other lunar meteorites with intermediate-iron bulk concentration in particular to those that are thought to be binary mixtures. These types of lunar meteorites are defined by Korotev et al. (2009) as mixtures of brecciated anorthosite from Feldspathic Highland Terrane and volcanic basalt from maria, with low contents of incompatible trace elements such as Sm (1–3 μg/g). Currently, only a few meteorites are part of this group: Meteorite Hills (MET) 01210 (Day et al., 2006); the YQN launch pair, that is, Yamato (Y) 793274/981031, Queen Alexandra Range (QUE) 94281, NWA 4884 and Elephant Moraine (EET) 87521/96008), Dhofar 1180 and NWA 3136 (Arai and Warren, 1999; Anand et al., 2003a; Korotev et al., 2003, Korotev and Zeigler, 2014). Mount DeWitt (DEW) 12007 has also been classified as a binary regolith breccia, containing Very Low Titanium (VLT) materials and magnesian feldspathic materials, with a suggestion of launch-paring

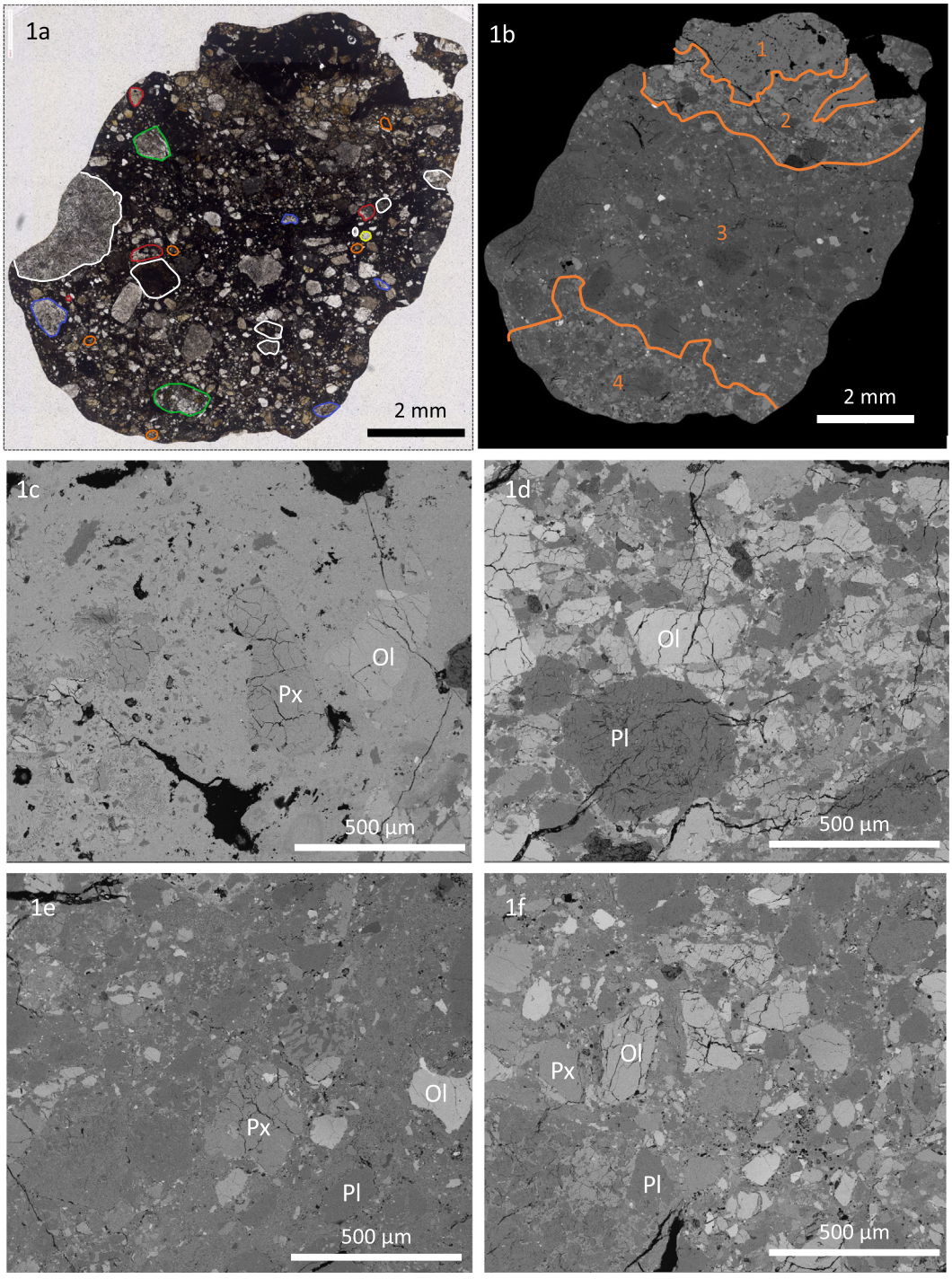

Fig. 1. Optical plane-polarized light (PPL) (1a) and BSE (1b) images of NWA 10989. On the optical image, lithic and impact melt clasts have been marked, each colour corresponds to a type of clast: white – impact melt clasts, red – mafic cumulate clasts, orange – evolved basaltic clasts, green – troctolite clasts, blue – norite clasts and yellow – granulite clast (higher magnification images of noteworthy clasts are shown in Fig. S1). On the BSE image, the four areas are highlighted (orange outlines) and are also presented in higher magnification below: 1c – Area 1; 1d – Area 2; 1e – Area 3; 1f – Area 4. Abbreviations stand for minerals: Ol-olivine, Px-pyroxene, Pl-plagioclase. Details are given in the text. (For interpretation of the references to colour in this figure legend, the reader is referred to the web version of this article.)

with the YQN group (Collareta et al., 2016). Newly classified lunar breccias NWA 7611 and NWA 7834 could also be added to this binary group (Ruzicka et al., 2015). NWA 10989 contains a higher abundance of feldspathic material than most of the YQN clan, but closer to Y-793274 (Warren and Kallemeyn, 1991; Arai and Warren, 1999), NWA 7611 and NWA 7834 (Ruzicka et al., 2015). It also contains very low regolith component compared to

the YQN clan, as indicated by the presence of vesicles (potentially relicts of agglutinates; cf. Fig. S2c).

3.2. Mineralogy

3.2.1. Major silicate minerals

Olivine occurs as euhedral grains which generally appear brown under PPL. Olivines share same characteristic as pyroxenes, i.e. most of the crystals are unzoned and are present throughout the thin section of NWA 10989, with a predominance in Areas 2 and 4. In total, 170 olivine analyses were collected from single mineral grains (n = 134) from the matrix, from lithic clasts (n = 27) and from impact melts (n = 9) across the studied thin section (available in Supplementary Table S13). Olivine Fo (Fo = molar (Mg/(Mg + Fe)) * 100) content varies between Fo_5-Fo_{76} with an average of $Fo_{58\pm15}$. Figure S3a shows a histogram of olivine Fo content, and it is apparent that there are 3 groups of olivines: $Fo_{5–15}$, $Fo_{31–50}$, $Fo_{59–76}$; the majority of olivines (n = 139) being relatively Mg-rich. The few fayalitic olivines (Fo_5–Fo_{15}) found in the section all belong to the evolved basaltic clasts, while the most Mg-rich olivines are found in the troctolitic clasts (Fo_{74} on average). The average Fe/Mn in olivine is 104 ± 11.

Pyroxene crystals occur as blocky crystals. Under PPL they appear white to light brown or green in colour. Under cross-polarised light (XPL), evidence for shock is seen in terms of undulose extinction and sub domains within grains, which would suggest a shock stage S3 based on the classification of Rubin et al. (1997). Most pyroxene grains exhibit exsolution lamellae which are 1–2 μm in width, suggesting slow cooling (Grove, 1982). Similar exsolution lamellae in pyroxene have been observed in VLT basalt clasts in EET 87521/96008, Y-793274, QUE 94281 as well as MET 01210 basaltic breccias, implying this feature, although rare, is common to VLT basalts (Jolliff et al., 1998; Anand et al., 2003a, Arai and Warren, 1999; Day et al., 2006). Pyroxenes occur throughout the thin section of NWA 10989, however, they are more common in Areas 2 and 4. In total, 196 pyroxene analyses were collected from single mineral grains from the matrix (n = 159), from lithic clasts (n = 20) and from impact melt clasts (n = 17) across the studied polished thin section (cf. Supplementary Table S14). Pyroxenes in NWA 10989 show an extensive variation in term of Ca-Mg-Fe composition (cf. Fig. 2a). Orthopyroxene/enstatite, pigeonite, augite and ferroaugite are all observed within our thin section with the total range in pyroxene composition varying between $Wo_{3–43}En_{5–75}Fs_{15–64}$. Mg-rich orthopyroxene and pigeonite ($Wo_7En_{65}Fs_{25}$–$Wo_{37}En_{41}Fs_{22}$) are dominant in feldspathic lithic clasts, revealing a ferroan anorthosite origin of these clasts (James et al., 1989), while Fe-rich augite ($Wo_{26}En_{27}$-Fs_{47}-$Wo_{41}En_{19}Fs_{40}$) are typically found in basaltic evolved clasts (Fig. 2b). Crystallization trends in the Ca-Mg-Fe diagram are typical of mare basalt, with crystallization of Al-rich pyroxenes, followed by pigeonites and augites (Fig. 2a). Al/Si vs Fe/Mg plot (Fig. 2c) shows that first-formed orthopyroxenes are Al enriched, while the pigeonite and augite have a constant low Al/Si ratio, due to plagioclase crystallization (Bence and Papike, 1972). Some pyroxenes show core to rim igneous zoning; for example, two pyroxenes in Area 2 have compositions which vary from

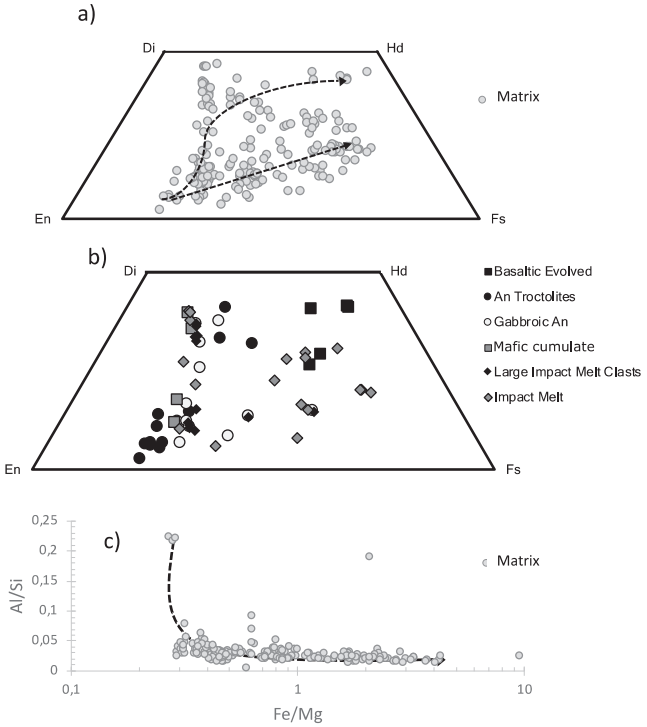

Fig. 2. (a) NWA 10989 matrix pyroxene compositions (b) Pyroxene compositions for individual lithic and impact-melt clasts. (c) Fe/Mg vs Al/Si of NWA 10989 matrix pyroxenes.

$Wo_8En_{42}Fs_{50}$ to $Wo_{35}En_{40}Fs_{25}$ and $Wo_5En_{64}Fs_{30}$ to $Wo_{12}En_{60}Fs_{29}$. However, the majority of pyroxene crystals are not zoned, which suggests sub-solidus re-equilibration. The average Fe/Mn in pyroxene is 64 ± 11.

Plagioclase feldspar occurs as both small and large grains (up to 1 mm in size), some are euhedral with 2:1 aspect ratios. Other grains are more rounded or irregular in shape suggesting that they have undergone some physical comminution. Although feldspar crystals occur throughout NWA 10989, they tend to be larger and more abundant in Area 3 of the breccia. Under PPL, feldspars appear as white to beige in colour, often with a dusty or speckled appearance. Small surface cracks are commonly seen across the crystal surface. Under XPL, most of large feldspar crystals show evidence for shock, such as partial maskelynitisation of the crystal, as well as the presence of impact melt within the crystals. Primary twinning is only observed in a few small crystals. According to the shock stage classification (Rubin et al., 1997), these features are consistent with the S3/S4 stage. Some of the larger (mm) feldspar crystals show evidence for fine-grained recrystallization and undulose or wavy extinction. In total 222 distinct EMPA data points were collected on feldspar grains, among which 178 were in the matrix, 24 in the lithic clasts and 20 in the impact-melt clasts (cf. Table S15). The variation in An component (An# = molar (Ca/(Ca + Na + K)) * 100) of these feldspar grains are displayed in an histogram in Figure S3b and in general, the measured An component ranges from An_{80} to An_{99}. This wide range of plagioclase composition in NWA 10989 overlaps with most of the compositional variations observed in felsdpathic and mare-basalt materials (Papike et al., 1991). Several crystals were observed to have lower An contents, including a small (~5 μm × 5 μm) crystal in Area 4 with An_{82}, and a ~0.5 mm crystal within Area 3 with An_{80}. There is generally no systematic variation in crystal composition across the sample, with most feldspars having a near average composition. All feldspar grains contain a low orthoclase (Or) component (molar (K/(Ca + K + Na)) * 100), with the maximum Or-component recorded as 2.5.

3.2.2. Minor phases

Oxide phases such as Al-Cr-rich spinels and ilmenite occur as sub-angular to sub-rounded grains within lithic clasts or as single mineral grains in the matrix. Ilmenite compositions do not show much variation throughout the sample with 40–45 wt.% FeO, 52–55 wt.% TiO_2, 0–3.5 wt.% MgO. All of the spinels are chromite, a few of which can be categorized as aluminium chromite with compositions varying between 35–45 wt.% Cr_2O_3, 7–17 wt.% Al_2O_3, 1–10 wt.% TiO_2, 2–5 wt.% MgO and 2–36 wt.% FeO. Figure S4 shows the 2Ti-Al-Cr ternary diagram, the Ti# vs. Fe# and Cr# vs. Fe# plots with a comparison with spinels from Apollo basalts and highlands samples. The spinel compositions bear a resemblance to both the Mg-Suite spinels as well as basaltic spinels (Papike et al., 1991).

Apatite is the only major phosphate mineral in this meteorite followed by minor merrillite. Apatite generally occurs as euhedral or blocky isolated mineral grains in the matrix, and has a size range of ~15–50 μm. The exceptions are an apatite crystal that occurs in association with a fayalite-hedenbergite-silica symplectite (cf. Figure S1b), and two apatites that are intergrown with merrillite at the crystal edges. These apatites are not associated with an impact melt or any other shocked phases, and as such they appear to display primary igneous textures with no evidence for recrystallization. Chemical composition of apatites as measured by EMPA is presented in Table 1. All apatites have a similar chemical composition, although apatite #10 is depleted in F and Cl compared to the other grains. SEM images of all apatites are presented in figure S5. One merrillite crystal was also found (Figure S5).

There is one occurrence of an Fe-Ni metal phase within the matrix, identified as kamacite (86 wt.% Fe, 8 wt.% Ni, 1 wt.% Co) and one occurrence of schreibersite (14 wt.% P, 74 wt.% Fe, 8 wt.% Ni; $(Fe,Ni)_3P$), in contact with olivine (Fo_{38}) and plagioclase (An_{90}) in Area 3.

3.3. Petrogenesis

3.3.1. Bulk composition

The whole-rock major- and trace-element composition of NWA 10989 as determined by INAA and ICP-OES/ICP-MS are presented in Table 2. Bulk-rock chemistry of NWA 10989 supports the intermediate nature of this lunar breccia, in agreement with petrologic observations of a roughly equal proportion of feldspathic and basaltic/mafic materials (e.g. 60:40). Firstly, FeO content (i.e. 12.6 ± 0.8 wt.% – INAA) and Al_2O_3 content (18.5 ± 0.3 wt.%) of NWA 10989 fall in the compositional criteria established by Korotev et al. (2009) (7–17% FeO, 13–20% Al_2O_3) for lunar breccia of intermediate-iron concentration. Secondly, the whole-rock chondrite-normalized rare earth element (REE) abundances (Fig. 3) show a typical signature of feldspathic-mare mixture with a slight negative Eu anomaly (Eu/Eu* = 0.67), and LREE enrichment compared to HREEs (e.g. ~ 39 × CI La and ~ 37 × Lu, La/Yb (CI-normalized) = 2.05). Finally, Fig. 4 shows Sm vs Sc plot that also positions NWA 10989 as a lunar meteorite of intermediate-iron composition. For the bulk-rock, the low Na_2O (i.e. 0.38–0.42 wt.%), K_2O (0.10 wt.%) and TiO_2 (0.59 wt.%) contents, as well as the low/medium Th content of 1.04 μg/g suggest a relatively minor contribution of KREEP-rich material to NWA 10989, consistent with petrographic observations. This low bulk-rock TiO_2 content also suggests that Ti-rich basaltic material is absent from this meteorite, again consistent with petrographic observations. Using the 'Apollo model' compositional end members from Korotev et al. (2009), a simple mass balance calculation suggested NWA 10989 to be a 45:52:3 mixture of mare:feldspathic:KREEP material. This is broadly comparable to the estimate made from petrographic observations (~40:60 ratio of mafic and feldspathic material). As such, it would appear that we have studied a polished section which is representative of the bulk sample. The bulk-rock Ir (4.3 ng/g – equivalent to 0.7% CM chondrite (Anders and Grevesse, 1989)) and Ni (189 μg/g) contents are low, suggesting a minimal contribution by meteoritic material.

The lunar meteorite NWA 10989 shows geochemical similarities to the anorthosite-basalt mixtures (i.e. the

Table 1
EMPA compositions of apatite analysed in NWA 10989. OH is calculated by stoichiometry.

Apatites #	1	2	4	7	9a	9c	9e	10a	10b
Formula									
wt.%									
P_2O_5	40.99	42.00	40.97	41.70	40.18	40.50	39.32	41.24	41.78
SiO_2	0.19	0.77	0.98	0.52	1.03	0.96	1.41	0.40	0.18
SO_2	0.03	0.09	0.02	0.10	0.08	0.08	0.10	0.09	0.06
Y_2O_3	0.27	0.16	0.23	0.03	0.22	0.34	0.11	0.30	0.33
Ce_2O_3	0.18	0.18	0.22	0.01	0.14	0.18	0.07	0.32	0.33
MgO	0.06	0.17	0.17	0.13	0.14	0.06	0.08	0.21	0.03
CaO	54.72	54.55	52.55	54.83	54.18	54.10	52.99	53.28	53.67
MnO	0.03	0.04	0.03	0.05	0.02	0.04	0.06	0.03	0.02
FeO	0.37	0.66	1.15	0.80	1.21	1.02	2.84	0.74	0.70
Na_2O	*bdl*	*bdl*	*bdl*	*bdl*	*bdl*	*bdl*	*bdl*	*bdl*	*bdl*
F	2.33	3.13	2.93	3.03	3.51	3.89	2.87	1.48	1.33
Cl	0.31	0.42	0.30	0.40	0.29	0.24	0.63	0.16	0.14
Total	99.49	102.2	99.55	101.6	101.0	101.4	100.5	98.25	98.57
$F_2 = O$-	0.98	1.32	1.23	1.28	1.48	1.64	1.21	0.62	0.56
$Cl_2 = O$-	0.07	0.09	0.07	0.09	0.07	0.05	0.14	0.04	0.03
O = F, Cl	1.05	1.41	1.30	1.37	1.54	1.69	1.35	0.66	0.59
Total	98.44	100.8	98.25	100.22	99.47	99.72	99.13	97.59	97.97
Stoichiometry based on 13 anions									
ppm									
P	2.96	2.96	2.96	2.96	2.90	2.91	2.85	2.97	3.00
Si	0.02	0.06	0.08	0.04	0.09	0.08	0.12	0.03	0.02
S	0.00	0.01	0.00	0.01	0.01	0.01	0.01	0.01	0.00
Y	0.01	0.01	0.01	0.00	0.01	0.02	0.01	0.01	0.01
Ce	0.01	0.01	0.01	0.00	0.00	0.01	0.00	0.01	0.01
Mg	0.01	0.02	0.02	0.02	0.02	0.01	0.01	0.03	0.00
Ca	5.00	4.87	4.81	4.93	4.95	4.93	4.88	4.87	4.88
Mn	0.00	0.00	0.00	0.00	0.00	0.00	0.00	0.00	0.00
Fe	0.03	0.05	0.08	0.06	0.09	0.07	0.20	0.05	0.05
Na	0.00	0.00	0.00	0.00	0.00	0.00	0.00	0.00	0.00
Σ cations	8.04	7.98	7.97	8.01	8.06	8.03	8.09	7.99	7.97
F	0.63	0.82	0.79	0.80	0.94	1.04	0.78	0.40	0.36
Cl	0.04	0.06	0.04	0.06	0.04	0.03	0.09	0.02	0.02
Σ anions	0.67	0.88	0.83	0.86	0.99	1.08	0.87	0.42	0.38
OH	0.33	0.12	0.17	0.14	0.01	−0.08	0.13	0.58	0.62
Mg#	22.42	31.47	20.85	22.46	17.10	9.49	4.78	33.59	7.10

YQN launch pairs, Dhofar 1180 and NWA 3136, DEW 12007, NWA 7611 clan, NWA 7834 clan; Korotev et al., 2009; Ruzicka et al., 2015). They contain very low incompatible trace elements such as Sm (1–3 μg/g) and thus do not contain a substantial KREEP component; in the case of NWA 10989 the estimated KREEP component is less than 3%. The YQN group that consists of VLT and magnesian felsdpathic components, are chemically very close to NWA 10989 (Korotev and Zeigler, 2014). Indeed, these meteorites plot on a mixing trend between VLT basalt and a nonmare (~feldspathic) component, more magnesian than any felsdpathic lunar meteorites (Korotev et al., 2003). In particular, NWA 10989 is extremely close to QUE 94281 which has a FeO content of ~13–14 wt.% and a Al_2O_3 content of 15.8 wt.% (Jolliff et al., 1998; Arai and Warren, 1999; Korotev et al., 2003), as well as its launch pair Y-793274/981031 because of the higher felsdpathic content of this meteorite compared to the other ones of the YQN group (Warren and Kallemeyn, 1991; Jolliff et al., 1998; Arai and Warren, 1999). Interestingly, it is also close to NWA 5651 (FeO = 12.7 wt.% and Al_2O_3 = 17.3 wt.%; Korotev et al., 2009) which is a fragmental to melt-matrix breccia (Korotev et al., 2009). Two other clans of lunar breccias, the NWA 7611 clan and particularly the NWA 7834 clan have composition closer to NWA 10989 (cf. Fig. 4, Ruzicka et al., 2015) than the YQN clan. For instance, NWA 7834 have a FeO content of 12.9 wt.% (compared to 12.6 ± 0.08 wt.% for NWA 10989), a Sc content of 25.0 μg/g (compared to 22.5–25.5 μg/g), Sm content of 3.1 μg/g (compared to 3.5–4.2 μg/g for NWA 10989) and a Th content of 0.9 μg/g (compared to 1.04–1.57 μg/g). This meteorite and its launch pairs are also feldspathic breccias, thus with lower mare material, suggesting that NWA 10989 could be another paired meteorite of NWA 7834 clan.

The bulk-rock REE signature of NWA 10989 also resembles those of other binary lunar breccias (Fig. 3). Some of these breccias: MET 01210, NWA 3136 and EET 87521 (Jolliff et al., 1998; Day et al., 2006; Korotev et al., 2009) have, however, REE patterns slightly different than NWA 10989, presumably on account of them having

Table 2
Bulk-rock major- and trace-element composition of NWA 10989. Data from ICP-OES/ ICP-MS and INAA are based on 3 replicates and 3 subsamples, respectively. Major-element oxide (except K_2O) as well as Cr concentrations were determined by ICP-OES, the rest of the elements, by ICP-MS. Mass-weighted data are reported for INAA. Variations in INAA and ICP-MS data are likely to be because of difference in relative proportion of felsdpathic vs basaltic clasts in subsamples, due to the intermediate nature of the sample (Korotev et al., 2009).

		ICP-OES/ICP-MS	stdev	INAA	stdev
Al_2O_3	wt%	18.5	0.3	–	–
CaO	wt%	12.5	0.2	12.1	0.6
FeO	wt%	11.0	0.1	12.6	0.8
K_2O	wt%	0.1007	0.0004	<0.2	
MgO	wt%	8.51	0.11	–	–
MnO	wt%	0.171	0.002	–	–
Na_2O	wt%	0.420	0.005	0.382	0.016
P_2O_5	wt%	0.1014	0.0010	–	–
SiO_2	wt%	44.9	0.3	–	–
TiO_2	wt%	0.589	0.009	–	–
Li	μg/g	9.05	0.08	–	–
Be	μg/g	0.788	0.013	–	–
Sc	μg/g	22.53	0.08	25.5	0.7
Cr	μg/g	1663	8	2154	231
V	μg/g	73.2	0.2	–	
Co	μg/g	37.5	0.1	45	3
Ni	μg/g	189.7	0.6	190	20
Cu	μg/g	8.49	0.08	–	
Zn	μg/g	18.4	0.2	–	
Ga	μg/g	3.83	0.07	–	
As	μg/g	0.419	0.018	0.32	0.19
Br	μg/g	–	–	0.38	0.26
Rb	μg/g	2.09	0.05	2.42	0.91
Sr	μg/g	167.4	0.6	181	49
Y	μg/g	27.3	0.1	–	–
Zr	μg/g	106.5	0.7	120	8
Nb	μg/g	7.18	0.06	–	–
Mo	μg/g	0.097	0.015	–	–
Cd	μg/g	0.154	0.009	–	–
Sn	μg/g	1.03	0.08	–	–
Sb	μg/g	<0.07	–	0.02	0.01
Cs	μg/g	0.102	0.009	0.06	0.01
Ba	μg/g	426	1	649	129
La	μg/g	9.06	0.07	7.88	0.93
Ce	μg/g	24.1	0.04	18.7	1.6
Pr	μg/g	3.373	0.007	–	–
Nd	μg/g	15.1	0.1	11.8	1.8
Sm	μg/g	4.19	0.02	3.46	0.23
Eu	μg/g	1.023	0.005	0.86	0.05
Gd	μg/g	5.13	0.07	–	–
Tb	μg/g	0.836	0.002	0.70	0.03
Dy	μg/g	5.59	0.02	–	–
Ho	μg/g	1.120	0.005	–	–
Er	μg/g	3.40	0.03	–	–
Tm	μg/g	0.464	0.003	–	–
Yb	μg/g	3.06	0.03	2.39	0.14
Lu	μg/g	0.423	0.005	0.34	0.01
Hf	μg/g	2.61	0.02	2.52	0.09
Ta	μg/g	0.352	0.007	0.27	0.02
W	μg/g	0.171	0.030	–	
Ir	ng/g	–	–	4.35	0.88
Au	ng/g	–	–	8.4	5.2
Tl	μg/g	0.0312	0.0010	–	–
Pb	μg/g	3.74	0.05	–	–
Th	μg/g	1.573	0.006	1.04	0.09
U	μg/g	3.054	0.005	0.55	0.14

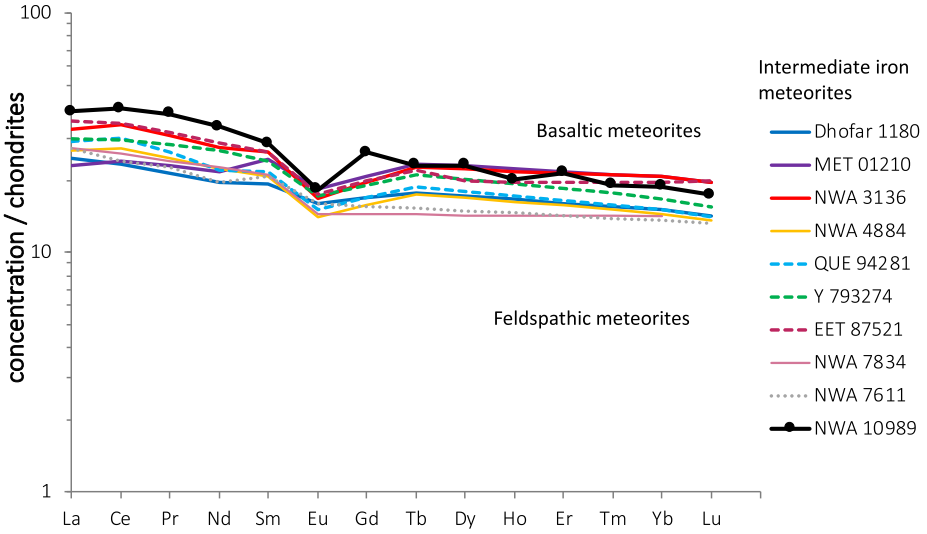

Fig. 3. Chondrite-normalized plot of REE concentrations of NWA 10989 based on ICP-MS data (ref. Table 2). The chondrite normalisation values are from Anders and Grevesse (1989). REE patterns of highlands meteorites (dark grey – Cahill et al., 2004; Korotev et al., 1996) and Apollo basalts as well mare basalt meteorites (light grey – Elardo et al., 2014) are also plotted. References of meteorite with intermediate-iron composition are from Jolliff et al. (1998) (QUE94281, Y793274, EET 87521), Korotev et al. (2009) (NWA 4882, NWA 3136, Dhofar 1180, MET 01210) and Ruzicka et al. (2015) (NWA 7834S, NWA 7611).

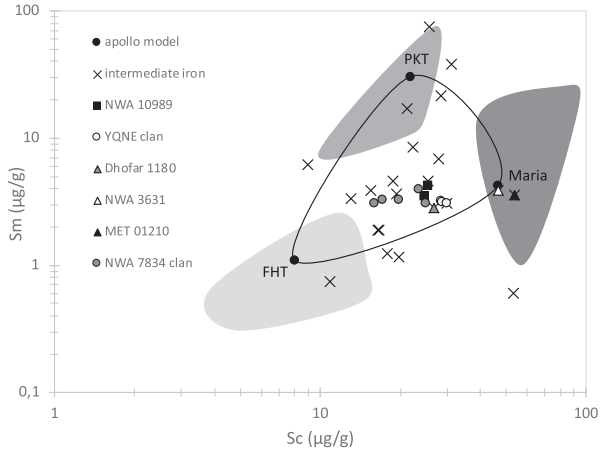

Fig. 4. Bulk-rock Sm versus Sc contents of NWA 10989. Other lunar meteorites have been plotted for comparison including the other meteorites of intermediate-iron composition (modified after Korotev et al., 2009).

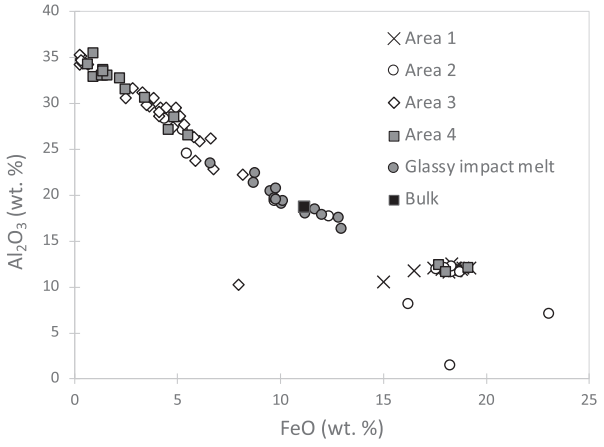

Fig. 5. Plot of Al_2O_3 versus FeO for matrix glasses and the large glassy impact melt from the 4 different areas of NWA 10989. The glasses exhibit a continuum from pure anorthositic to basaltic composition. The bulk-rock composition of NWA 10989 is also plotted.

higher abundances of VLT basaltic material relative to felsdpathic material (i.e. ~70–80% VLT; Korotev and Irving, 2005).

In the following sections, we discuss composition of the basaltic material, predominantly in Areas 2 and 4; and composition of felsdpathic material of NWA 10989, mainly represented in Areas 3 and 4 (cf. Fig. 1) by impact melts, lithic clasts and matrix components.

3.3.2. Basaltic materials

Basaltic material is represented by impact melts, matrix glasses, and mineral fragments in the matrix, as the majority of lithic clasts show an affinity to felsdpathic rocks. Al_2O_3 vs FeO content of matrix glass and a glassy-impact-melt breccia clast are plotted in Fig. 5, as a function of their location throughout NWA 10989 (cf. Areas 1, 2, 3, 4 – Fig. 1). The glass composition of Area 1 (Table S5) shows limited variation and its average composition of 1.15 ± 0.07 wt.% TiO_2, 18.0 ± 1.06 wt.% FeO and 11.8 ± 0.42 wt.% Al_2O_3 ($N = 15$, 2σ) is similar to VLT basalts (Vaniman and Papike, 1977, Neal and Taylor 1992). Most of the Area 2 glasses have a similar VLT composition (1.03 wt.% TiO_2, 18.5 wt.% FeO, 9.4 wt.% Al_2O_3; $n = 8$), while some of Area 2 glasses exhibit extreme values of FeO (23 wt.%) and Al_2O_3 (1.34 wt.%) contents. As such, matrix glasses in NWA 10989 appear to be a mixture of basaltic components, with an important contribution of VLT-type

precursor reservoir. As stated previously, the low K_2O content (0.10 wt.%) of the bulk-rock suggests a relatively minor KREEP component, which in this instance is not carried by basalts. Indeed, KREEP-rich basalts are classified based on their high bulk-rock K_2O content (> 0.2 wt.%; Taylor et al., 1991; Neal and Taylor, 1992), while basalt clasts in NWA 10989 have K_2O content lower than 0.1 wt.%.

The Fe# vs. Ti# of pyroxenes characterize trends indicative of parent magma composition (Nielsen and Drake, 1978). Two major trends on Fe# vs Ti# plot are observed among the pyroxene fragments analysed in NWA 10989 matrix, as well as the pyroxene grains within lithic clasts and impact-melt clasts (Fig. 6). The main trend defines a correlation between Ti# and Fe#, typical of basaltic magmas, and is similar to that seen for VLT basalts as meteorite data plot close to the trend defined by Apollo 17 (Vaniman and Papike, 1977) and Luna 24 (Nielsen and Drake, 1978; Meyer et al., 1978) VLT basalts. Pyroxenes in NWA 10989 that fall on the VLT trend show also low alkali contents typical of Apollo 17 VLT pyroxenes ($Na_2O + K_2O < 0.2$ wt.%; Vaniman and Papike, 1977). However, Ti# and Fe# of NWA 10989 pyroxenes do not define a single magmatic field but the data are scattered across fields defined by the mare basalts. These basaltic pyroxenes can be separated in two sub-trends, one of more mafic (i.e. Fe# < 0.5) and one of more ferroan (Fe# > 0.6) types. These two sub-trends have been observed previously in the basaltic polymict breccia Y-793274 (Arai et al., 1996). Indeed, these trends are presented for all breccias of the YQN clan (Arai and Warren, 1999; Anand et al., 2003a; Korotev et al., 2003, Korotev and Zeigler, 2014), as well as presented in other intermediate-iron bulk composition breccias such as MET 01210 (Day et al., 2006). Mineralogically, the composition of pyroxenes from NWA 10989 show similarity with VLT materials of EET98/96 and Y-793274 from the YQN clan, albeit pyroxenes in NWA 10989 contain ~1 wt.% less Al_2O_3. Moreover, the relatively thick exsolution lamellae (~1 μm) in pyroxenes are also observed in basaltic clasts of EET 87521/96008, Y-793274, QUE 94281 as well as MET 01210 (Jolliff et al., 1998; Anand et al., 2003a, Arai and Warren, 1999; Day et al., 2006; Arai et al., 2010).

The rest of matrix, impact melt and most of lithic clast pyroxenes show another trend on Fig. 6, with a restricted range of Fe# (~0.3–0.4) with more scatter but higher Ti# (0.5–0.9), similar to Fe-poor and Ti-rich pyroxenes observed in felsdpathic rocks (Arai et al., 1996; Papike et al., 1991; Joy et al., 2011). Furthermore, based on major-element composition, matrix glasses are predominantly of felsdpathic composition (Fig. 5).

Using the correlation between bulk-rock TiO_2 content of low-Ti mare basalt and pyroxene $Ti\#_{0.5}$ (i.e. the Ti# of pyroxene at fixed Fe# = 0.5) defined by Arai et al. (1996), we estimated the bulk TiO_2 content of NWA 10989 basaltic source. As shown in Fig. 7, pyroxenes of NWA 10989 predict a parent magma composition containing 1.0 ± 0.2 wt.% TiO_2. This estimated value is higher than the bulk-rock TiO_2 content determined by ICP-OES (0.6 wt.%; Table 2). This relatively large difference is almost certainly a result of the intermediate nature of NWA 10989, and consequently to the large amount of felsdpathic material that was represented in the measured bulk composition. Moreover, this estimated bulk magma TiO_2 content is similar to the average bulk TiO_2 content of the impact melt glass measured in Area 1 (i.e. 1.15 ± 0.07 wt.% TiO_2), as well as most of glasses in Area 2. The Area 1 impact melt is thus postulated to be representative of the bulk composition of the VLT basalt component in this meteorite (Table S5), characterized by TiO_2 content of ~1 wt.%. This number is comparable to estimation made for the YQN basaltic meteorite group (Arai et al., 1996; Arai and Warren, 1999; Anand et al., 2003a), confirming NWA 10989 being a mixture of mare basalts, with an important contribution derived from melting of VLT basaltic reservoir.

3.3.3. Feldspathic materials

The felsdpathic composition is characterized by impact-melt clasts, glasses, mineral fragments and also most of lithic clasts. From the EMPA analyses on the matrix glasses (cf. Table S5) in Area 3, which constitutes ~64% of the section, and Area 4 account for majority of the feldspathic components in the meteorite. They define a linear contin-

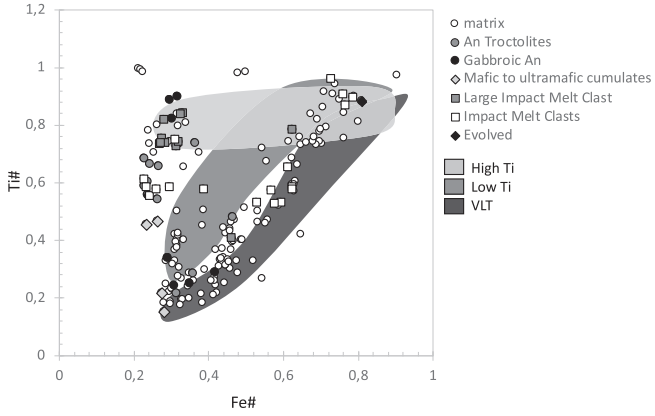

Fig. 6. Plot of #Fe versus #Ti for pyroxenes in the evolved basaltic clasts, impact-melt class and matrix. Area representing typical pyroxenes compositions for VLT, low-Ti and high-Ti lithologies are shown as envelopes using different shades of grey. The VLT field outlined includes the data for Apollo 17 VLT pyroxenes (Vaniman and Papike, 1977), Luna 24 pyroxenes (Meyer et al., 1978) and pyroxenes from several lunar meteorites (Arai et al., 1996; Anand et al., 2003a).

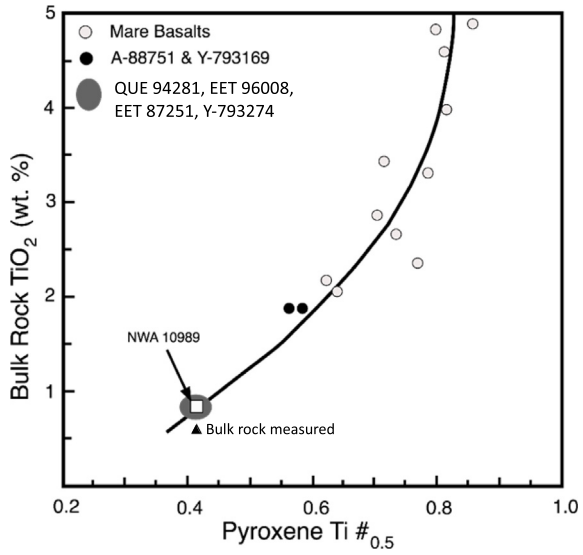

Fig. 7. Plot of Fe#-normalized pyroxene Ti# versus bulk-rock TiO_2 content for Apollo mare basalts and basaltic meteorites (modified after Arai et al., 1996; Anand et al., 2003a).

uum from feldspathic, with $Al_2O_3 \sim 35$ wt.%, CaO ~ 19 wt. %, FeO and MgO below detection limit, to mafic, with MgO ~ 10 wt.%, $Al_2O_3 \sim 16$ wt.%, CaO ~ 11 wt.%, FeO ~ 13 wt.% (cf. Fig. 5). This linear trend is likely to represent a mixing between nearly pure anorthosite and a more mafic end member. Within Area 2, a few feldspathic points were measured, plotting on the more mafic side of the trend (23.3 wt.% Al_2O_3, 7.4 wt.% FeO).

Several measurements made across a glassy impact clast (up to 750 µm; Figure S2), give an average composition (N = 14) of 19.5% Al_2O_3 and 10.3% FeO, similar to the noritic end of glass composition. This mafic end member of the linear trend does not correlate with any known Apollo glass composition. However, it is compositionally similar to the noritic glasses reported in PCA 02007 (i.e. ~18 wt.% Al_2O_3, ~14 wt.% FeO; Day et al., 2006; Joy et al., 2010), the norite composition in 77215 (Chao et al., 1976) and the glass vein found in QUE 94281 (i.e. 20 wt. % Al_2O_3, 11 wt.% FeO; Jolliff et al. 1998).

The average An# of plagioclase is plotted as a function of the average Mg# of associated mafic minerals (i.e., olivine and pyroxene) for each feldspathic clast and impact-melt clast (Fig. 8). The four gabbroic anorthosites and anorthositic gabbros show an affinity to Ferroan Anorthositic (FAN) composition, typical of Apollo 16 samples (McGee, 1993) but rarer for lunar felsdpathic breccia (Gross et al., 2014). The two anorthositic troctolites fall in between the FAN suite and the Mg-suite, as seen among many lunar meteorites (Gross et al., 2014). Indeed, it has been observed that mixed meteorites contain more sodic plagioclase and less mafic silicates than pristine highland Mg-suite rocks and FAN rocks (Demidova et al., 2007). The large impact melt has a similar FAN composition than the gabbroic anorthosites and anorthositic gabbros, and is probably derived from a similar FAN reservoir. Finally, for the impact-melt clasts, one plot along the Mg-suite trend, due to the more sodic nature (~An_{90}) of their feldspars, which is again not so common among felsdpathic meteorites (Gross et al., 2014). The others are like the troctolites, in between the range of Mg-suite and FAN suite. The feldspathic material in NWA 10989 tends to be associated with slightly more mafic minerals than typical Apollo 16 anorthositic highlands material, similar to the highly magnesian anorthositic trend identified in the majority of feldspathic meteorites (Gross et al., 2014). Thus, the majority of the felsdpathic material from NWA 10989 appears to be derived from two sources, one being derived from FAN material while the other plots in the mafic range of Apollo 16 FAN material.

3.4. Apatites and merrillite: volatile composition and age dating

3.4.1. Chlorine abundance and isotopic composition

In total nine measurements were made across six apatite grains from this meteorite. The chlorine isotope measurements and abundances are plotted in Fig. 9, and presented in Table 3. All apatite occur as isolated grains in the matrix, with no definitive petrographic context, except for apatite 9 which was located inside the symplectite clast (cf. Figure S5). The matrix apatite show a limited range in $\delta^{37}Cl$ between +14.4 and +18.7‰ with an average value of +15.9 ± 1.5‰ (2SD). Chlorine contents vary between 1270 and 4880 ppm with an average value of 2700 ± 1540 ppm. The apatite grain 9 in the symplectite clast displayed a range in $\delta^{37}Cl$ and Cl contents. The core of the crystal exhibits $\delta^{37}Cl$ of 11.9 ± 0.9‰ and 2700 ± 200 ppm Cl (average of 9a and 9c – Table 3), while the rim is more Cl rich (i.e. 6050 ± 630 ppm Cl), associated with heavier $\delta^{37}Cl$ value of 16.8 ± 1.5‰.

3.4.2. Hydrogen abundance and isotopic composition

Hydrogen isotopic ratio and concentration were also measured in eight apatites, among which six of them were also analysed for chlorine (cf. Table 3), and one merrillite (#11), as shown in Fig. 10. In total, seven out of nine phosphates exhibit low δD signatures, with values ranging from −420 ± 90 to +210 ± 90‰. Water content associated with these apatites range from +260 ± 20 to +1580 ± 120 ppm H_2O. On the other hand, apatites #1 and #10, show high water contents of 0.3 and 0.9–1 wt.% H_2O, respectively, along with one of the highest ever measured δD in an apatite from a lunar meteorite apatite (from +410 ± 70 to +1010 ± 90‰) (Tartèse et al., 2013). It should be noted that these H_2O measurements are not similar to the OH determined by stoichiometry in Table 1, which is most likely because of overestimation of F by EMPA. No spallation correction has been made on these analyses as the CRE age of NWA 10989 is currently unknown. However, Tartèse et al. (2014) estimated that based on the older CRE age of lunar polymict breccia NWA 4472 (i.e. 2 ± 0.2 Ga, Lorenzetti, 2005), for an apatite containing ~1800 ppm H_2O, the maximum correction for δD is ~60‰. Although in some cases, the measured water contents are lower than 1800 ppm, we assume that the spallation correction is within our stated uncertainties of each

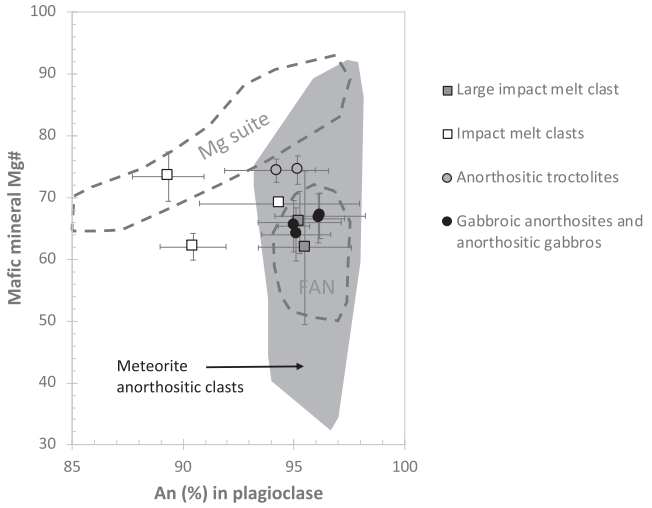

Fig. 8. Average An# in plagioclases as a function of average Mg# of associated mafic minerals (olivines and pyroxenes) in impact-melt clasts and feldspathic lithic clasts. Each marker represents a single clast, except for the large impact-melts where markers represent two areas. Errors associated are standard deviation of both plagioclase An# and mafic mineral Mg# in the clast. The areas of FAN and Mg suite are delineated with grey dashed lines and are from Papike et al. (1998). The grey area represents meteorite anorthositic clasts and are from Gross et al. (2014).

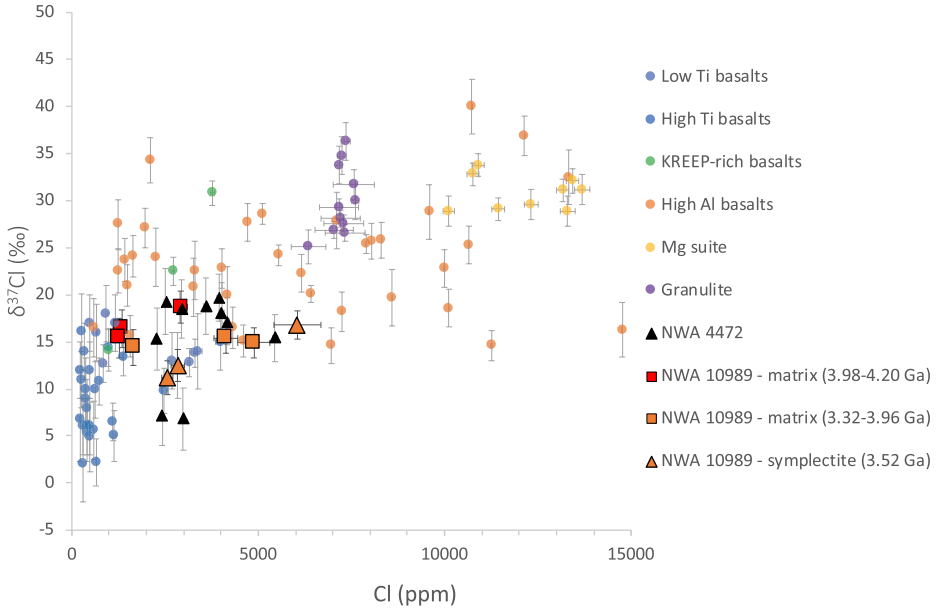

Fig. 9. Chlorine isotopic composition (‰) and contents (ppm) in NWA 10989 compared to lunar meteorite NWA 4472 and to Apollo samples. Red symbols are for NWA 10989 apatites with ages ranging from 3.98 to 4.20 Ga while orange symbols are for apatites with ages ranging from 3.32 to 3.96 Ga. Squares represent NWA 10989 matrix apatites, while triangles represent the symplectite apatite. Lunar meteorite data are from Tartèse et al. (2014); Apollo data are from Boyce et al. (2015), Barnes et al. (2016), Potts et al. (2018).

measurement. In any case, we recommend that the reported δD values for low-water apatite be treated as the upper limit as the corrected δD values will be displaced towards lighter values. Lunar meteorites are susceptible to terrestrial contamination and therefore often display δD values closer to terrestrial water (Tartèse et al., 2013). However, (i) the relatively high water concentrations in apatites (Stephant et al., 2018), (ii) the high δD values of phosphates compared to terrestrial δD value, as well as (iii) the lack of any apparent terrestrial contamination trend on the δD vs H_2O graph, allows us to rule out any major terrestrial contamination affecting the H isotope systematics of phosphates this sample.

3.5. Lead-lead (Pb-Pb) age of apatites and merrillite

Ages of apatites was carried out in this study using Pb-Pb method (Table 4). The concentrations of U and Th in

Table 3
Chlorine and hydrogen isotopic ratios expressed in delta values (‰), along with Cl, F, H_2O ppm abundances and the Pb-Pb dates of 9 apatites from NWA 10989. Apatite 9 is from a symplectite (Figure S1b) while the other apatites are from the matrix. $\delta^{37}Cl$, Cl content, F content and δD, H_2O content were measured in 2 different NanoSIMS sessions (see methodology for details).

Phosphates	Age (Ga)	$\delta^{37}Cl$ (‰)	2σ	Cl (ppm)	2σ	F (ppm)	2σ	H_2O (ppm)	2σ	δD (‰)	2σ
1 (Ap.)	4.20 ± 0.01	18.70	1.70	2920	180	23,490	210	3350	260	410	70
2 (Ap.)	3.35 ± 0.01	15.40	1.60	4130	320	28,020	250	800	60	100	90
4 (Ap.)	3.32 ± 0.01	14.40	1.90	1650	80	30,330	270	410	30	−420	90
4b (Ap.)	3.32 ± 0.01					–	–	660	50	−270	80
5 (Ap.)	–					–	–	1580	120	−110	60
7 (Ap.)	–	14.90	1.60	4880	430	27,450	240	1370	100	−20	60
8 (Ap.)	3.62 ± 0.02					–	–	260	20	−250	120
9a (Ap.)	3.52 ± 0.01	12.50	1.70	2840	180	30,390	270	1000	80	170	90
9c (Ap.)	3.52 ± 0.01	11.20	1.80	2560	150	31,090	280	660	50	10	90
9e (Ap.)	3.52 ± 0.01	16.80	1.50	6050	630	26,390	230	990	80	210	90
10a (Ap.)	3.98 ± 0.04	16.40	2.00	1340	70	12,150	110	9490	730	960	90
10b (Ap.)	3.98 ± 0.04	15.40	2.1	1270	60	11,790	100	8890	680	1010	90
10c (Ap.)	3.98 ± 0.04					–	–	9820	750	660	80
11 (Me.)	3.96 ± 0.03					–	–	750	60	−400	60

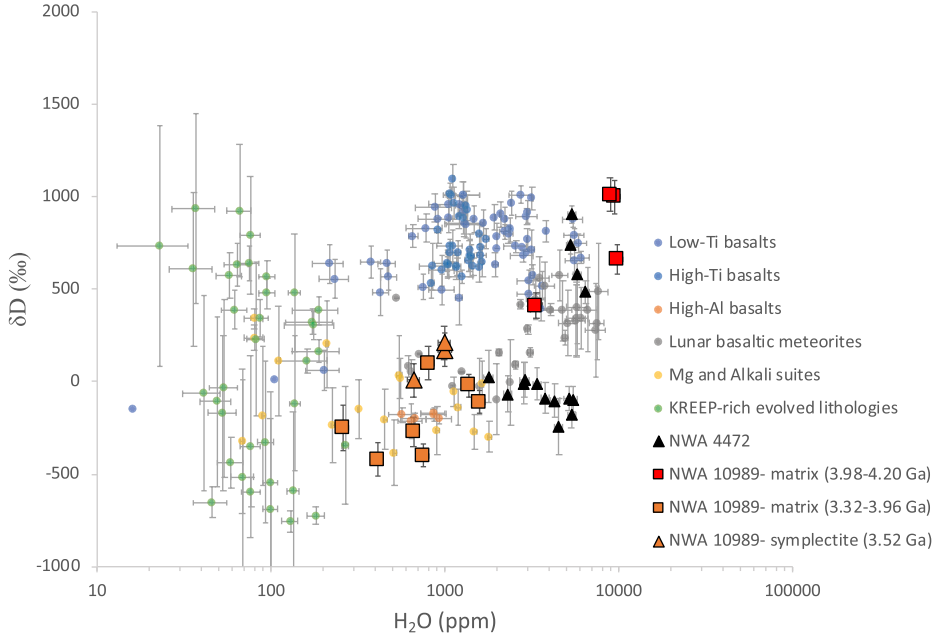

Fig. 10. Plot of δD (‰) versus H_2O content (ppm) of apatites in lunar rocks. Data for High and Low-Ti basalts are from Greenwood et al. (2011), Tartèse et al. (2013), Barnes et al. (2013); High-Al basalt data are from Greenwood et al. (2011); basaltic meteorites data are from Tartèse et al. (2013) and Tartese et al. (2014); NWA 4472 data are from Tartèse et al. (2014); Mg and alkali-suites data are from Barnes et al. (2014) and data for KREEP-rich evolved rocks are from Robinson et al. (2016). The legend is same as in Fig. 9.

Table 4
Concentrations of U and Th (ppm), $^{207}Pb/^{235}U$ and $^{206}Pb/^{238}U$ ratios and $^{207}Pb/^{206}Pb$ ages of NWA 10989 apatite.

Phosphates	U (ppm)	Th (ppm)	f_{206}%	^{206}Pb (c/s)	^{207}Pb ^{235}U	±σ %	^{206}Pb ^{238}U	±σ %	p	^{207}Pb ^{206}Pb age	±σ
Ap1 (Ap.)	25	32	{0.22}	340,389	71.53	1.76	1.07	1.54	0.87	4200	13
Ap2 (Ap.)	87	125	{3.04}	625,2057	27.11	1.78	0.71	1.54	0.87	3352	14
Ap4 (Ap.)	187	416	{0.15}	1173,271	20.89	1.72	0.56	1.62	0.94	3323	9
Ap8 (Ap.)	16	36	{1.60}	150,2539	31.25	2.25	0.69	1.72	0.76	3615	22
Ap8 (Ap.)	25	62	{1.17}	226,4088	41.09	3.07	0.91	2.06	0.67	3610	35
Ap9 (Ap.)	65	133	{0.46}	542,4333	27.30	1.75	0.64	1.58	0.90	3520	12
Ap10 (Ap.)	12	16	{7.12}	120,1721	40.61	3.23	0.70	1.52	0.47	3984	42
M11 (Me.)	40	640	{0.50}	381,3377	42.80	2.54	0.75	1.51	0.59	3962	30

apatite range from 12 to 187 ppm and 16 to 406 ppm, respectively, with Th/U ratios in the range of 1.3–2.5. The single merrillite has a U and Th concentrations of 40 and 640 ppm, respectively, which gives a Th/U ratio of 15.8. The Pb-Pb ages are discordant from the concordia curve and apatites do not define one discordia line. As such, these phosphates probably have experienced some Pb loss due to a shock event and do not seem to have a single crystallization age. If Pb was lost from apatites, their true crystallization age will be higher than the recorded Pb-Pb age. Apatites #1 and #10, defined as "typical" mare basalt apatites based on δD-δ^{37}Cl systematics (Fig. 11), have older Pb-Pb age than the rest of the apatites at 4200 ± 13 and 3984 ± 42 Ma, respectively. The rest of NWA 10989 apatites and the merrillite, similar to typical Mg and Alkali suite in terms of δD-H_2O systematics, record younger Pb-Pb ages from 3323 ± 9 to 3962 ± 30 Ma.

4. DISCUSSION

4.1. Lunar origin

Several lines of evidence have been used to confirm a lunar origin for NWA 10989. First of all, the Fe/Mn ratios of mafic minerals, i.e. olivines and pyroxenes, commonly used to discriminate between different planetary sources (Papike et al., 1998), are consistent with the known lunar trends (Karner et al., 2003, Karner et al., 2006) (Figure S6). Secondly, bulk-rock oxygen isotope analysis of this meteorite yielded the following values: $\delta^{17}O$ 3.42‰, $\delta^{18}O$ 6.51‰, $\Delta^{17}O$ 0.01‰. The oxygen isotopic composition of NWA 10989 plots on the terrestrial fractional line (Fig. 12), although the $\delta^{17}O$ and $\delta^{18}O$ values are shifted towards slightly higher values compared to those for Apollo samples (Hallis et al., 2010; Wiechert et al., 2001; Spicuzza et al., 2007; Herwartz et al., 2014; Young et al., 2016). Indeed, the oxygen isotopic composition of NWA 10989 is in the range of lunar meteorites (Fig. 12), in which the elevated oxygen isotopic values could be ascribed to presence of terrestrial weathering products formed in hot-desert environments (Stelzer et al., 1999; Anand et al., 2003b; Pillinger et al., 2013); NWA 10989 is also a hot-desert meteorite but its terrestrial residence time is currently unknown. Finally, the similarity between the mineralogy and geochemistry of minerals and lithic fragments seen in NWA10989 to Apollo and other lunar meteorite samples provides further evidence for a lunar origin.

4.2. Volatile reservoirs recorded by NWA 10989 phosphates

4.2.1. Implications of apatite and merrillite volatile compositions

Apatite δ^{37}Cl values (average ~ 16‰) in NWA 10989 are towards the higher range of mare basalt apatites, which range from −4 to +18‰ (Fig. 9) (Sharp et al., 2010, Boyce et al., 2015, Barnes et al., 2016) and towards the lower range of high-Al basalts, which range from +14 to +40‰ (Sharp et al., 2010; Tartese et al., 2014; Barnes et al., 2016; Potts et al., 2018). As such, NWA 10989 apatites most probably are of mare-basalt heritage, as they are rarely found associated with felsdpathic lithologies, and, the lack of KREEP-rich basaltic component in NWA 10989 precludes a common reservoir with high-Al basalts. The matrix apatites exhibit similar Cl signature to another lunar meteorite NWA 4472 (Tartèse et al., 2014). While this meteorite is also considered to be a breccia of intermediate-iron concentration (Korotev et al., 2009), its petrology differs from NWA 10989 in the sense that NWA 4472 is a

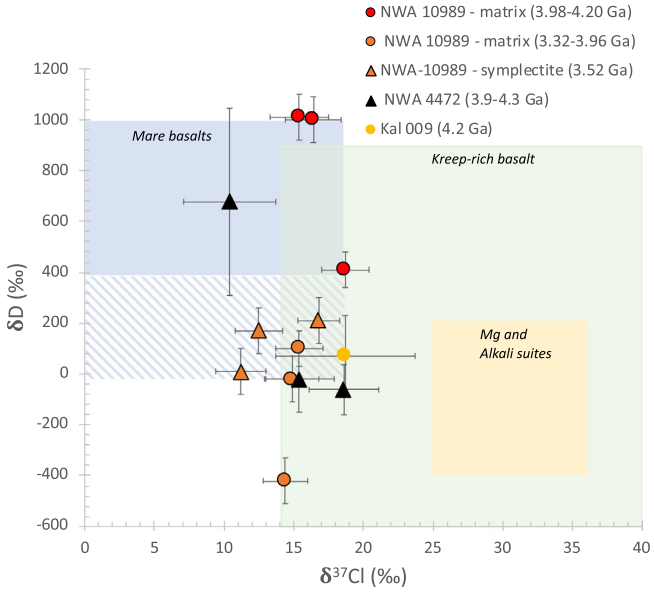

Fig. 11. Values of δD versus δ^{37}Cl (‰) recorded in NWA 10989 apatites. For comparison, NWA 4472 and Kal 009 apatites are also plotted (average and standard deviation – Tartèse et al., 2014, Barnes et al., 2019) as well as the area defined by samples from Apollo mission (Boyce et al., 2015, Greenwood et al., 2011; Barnes et al., 2013; Tartèse et al., 2013; Barnes et al., 2014, Robinson et al., 2016; Barnes et al., 2016). The legend is same as in Fig. 9.

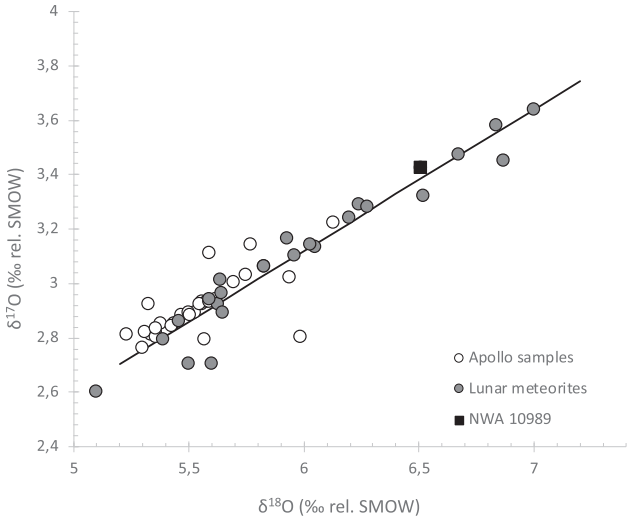

Fig. 12. The oxygen isotopic composition of NWA 10989 plots along the terrestrial fractionation line, also defined by other lunar meteorites (cf. Meteoritical Bulletin) and Apollo samples (Wiechert et al, 2001). NWA 10989 has slightly heavier isotopic values than other lunar meteorites, comparable to Dhofar 287A (Anand et al., 2003b).

KREEP-rich breccia (Joy et al., 2011), containing Mg-suite, alkali-suite, mare basalt and KREEP basalt lithologies.

The increase of Cl content from core to rim of the apatite in the symplectite appears consistent with fractional crystallization. The slight increase of $\delta^{37}Cl$ observed between core and rim could be explained by magmatic degassing of metal chlorides, although the difference remains within the variation observed among all the apatites in this meteorite. The reason for heavy lunar $\delta^{37}Cl$ compared to terrestrial value was first suggested to be due to degassing of the lunar magmas during and upon eruption (Sharp et al., 2010), which would be consistent with slight increase of $\delta^{37}Cl$ observed between core and rim of apatite 9. More recent studies have advocated for a mixing between two isotopic reservoirs: one with an elevated signature (i.e. +25 to +30‰) originally associated with the urKREEP reservoir and another with a lighter signature (~0‰) representative of mare-basalt source regions (Boyce et al., 2015; Barnes et al., 2016).

Apatites in NWA 10989 form two clusters in term of their H_2O-δD systematics (Fig. 10). These clusters may appear at first as a positive trend, implying that a magmatic or secondary process affected apatites from a single volatile reservoir. However, H_2 degassing of melts from a single reservoir would induce a negative trend and no known magmatic process could explain this trend. Moreover, no such trend is observed for chlorine systematics, which clearly ruled out any type of magmatic degassing. As stated previously, we do not expect a spallation contribution higher than 60‰ suggesting that these two clusters could in fact be signatures of two distinct volatile reservoirs. Finally, implantation of solar wind may play a role (Treiman et al., 2016) in lowering δD signatures of a basaltic melt, but tin such case, we would expect all apatites to have being affected. As such, we propose that these two clusters are indeed a signature of two distinct volatile reservoirs.

The δD-H_2O systematics of apatites #1 and #10 are in the range of what has been measured for Apollo mare basalts, i.e. high δD (>~+500‰) (Tartèse et al., 2013; Barnes et al., 2013), in agreement with their chlorine isotope signature (Fig. 11). However, the other six apatites and the merrillite with lower δD values (i.e. <~+200‰) and lower H_2O contents (i.e. < ~1600 ppm) fall in the δD-H_2O systematic range of values measured previously for Mg- and alkali-suites (Barnes et al., 2014; Greenwood et al., 2011) (Fig. 10), i.e. a low-δD reservoir, while their chlorine signature indicate a basaltic reservoir. Indeed, their chlorine isotope signature are similar to "typical" Apollo mare basalts (Sharp et al., 2010; Boyce et al., 2015; Barnes et al., 2016), and no characteristic $\delta^{37}Cl$ signature associated with highland material (e.g. ~+30‰, has been recorded in δD-poor apatites from Apollo samples). Moreover, as stated previously, it is unlikely that phosphates sampled a feldspathic reservoir. Indeed one of these apatites is located in the symplectite, which represents an evolved basaltic clast. It should be noted that three apatites in low-Ti mare basalt 12040 have been reported (Boyce et al., 2015; Treiman et al., 2016) to have lower δD values than seen in typical mare basalt. However, because of extremely low water contents in these apatites, only one analysis could be considered significant, with a δD value of −20 ± 200‰. At this stage, it is tenuous at best to make any detailed comparisons with this single data point, and additional data on this sample are required. Regardless, 12040 most probably sampled a different low-δD reservoir than NWA 10989, as the lack of KREEP component places the source region for this lunar meteorite far from Apollo landing sites. However, two basaltic meteorites, the monomict VLT breccia Kalahari 009 and the KREEP-rich breccia NWA 4472 have similar δD-H_2O systematics (Tartèse et al, 2014). Interestingly, the polymict lunar breccia NWA 4472 also displays similar clustering in Cl and H isotope space (Tartèse et al., 2014) (cf. Fig. 11). These two

clusters have been associated with two different reservoirs in the Moon, i.e. mare-basalt source regions for which the elevated δD values in apatites are thought to be a result of magmatic degassing and KREEP-rich basaltic reservoir associated with low-δD apatites. Therefore, at first, it would seem likely that apatites from both NWA 10989 and NWA 4472 sampled similar reservoirs for Cl and H. However, as stated before, NWA 4472 is a KREEP-rich breccia (Joy et al., 2011) while NWA 10989 has relatively low KREEP component (<3%). Moreover, apatites from KREEP-rich lithologies have even lower H_2O content than what is recorded in NWA 10989 apatites (Robinson et al., 2016; cf. Fig. 10), which are more similar to apatite water contents in Mg and alkali suite lithologies (Barnes et al., 2014).

4.2.2. Combination of phosphate volatile compositions and age dating

Age dating of apatites and merrillite can help us investigate further the potential lunar reservoirs sampled by NWA 10989 (Table 4), although these Pb-Pb ages have to be interpreted with caution as they may not represent true crystallization ages. In case of NWA 10989 apatites, there is no obvious evidence for shock (e.g. no association with other shocked phases or impact melt) which could have reset the Pb-Pb ages. Apatites #1 and #10, defined as "typical" mare basalt apatites based on δD-δ^{37}Cl systematics (Fig. 11), have older Pb-Pb ages compared to the rest of the apatites at 4.20 and 3.98 Ga, respectively. Thus, they are considered relics of old basaltic volcanism (cryptomare) on the Moon, as crystallization ages for majority of mare-basalts range from 2.9 to 3.9 Ga; the oldest mare basalt (thought to be a sample of cryptomare) sample being recorded by the monomict VLT breccia Kalahari 009 (Terada et al., 2007; Snape et al., 2018) at 4.35 Ga. The "typical" mare basalt apatites in NWA 4472 has also recorded an old crystallization age of 4.35 Ga similar to Kal 009 (Joy et al., 2011; Tartèse et al., 2014). However, while NWA 4472 and NWA apatites #1 and #10 have similar δD-δ^{37}Cl systematics, apatites in Kal 009 have a low δD signature, suggesting that these three meteorites (i.e. Kal 009, NWA 4472 and NWA 10989) contain components of ancient volcanic materials on the Moon that either had a distinct source region characteristic for H and Cl isotopes or post-magmatic processes affecting isotope fractionation were different than envisaged for Apollo samples.

The rest of NWA 10989 apatites and merrillite with low δD record younger ages from 3.32 to 3.96 Ga. These ages correspond to the main phase of mare-basalt magmatism, as Mg and alkali-suite samples generally have crystallization ages older than 4.17 Ga (Shearer et al., 2015). These Pb-Pb ages are also younger than ages reported for KREEP-rich basaltic components in NWA 4472 (i.e. 3.93–4.07 Ga; Joy et al., 2011), yet they have similar H and Cl isotope composition. Moreover, the average Th and U contents of NWA 10989 apatites are 57 and 183 μg/g, respectively, similar to apatite in lunar basaltic meteorites EET96008 and LAP 02205 (Anand et al., 2003a; Anand et al. (2006)), which are higher than in apatite from anorthositic material (Norman and Nemchin, 2014). Thus, the Th and U contents, added to the chlorine isotopic composition and the ages of these seven apatites, are in agreement with a mare heritage. As such, if these apatites are indeed from a mare source as most pieces of evidence seem to indicate, it highlights the existence of a mare reservoir which is depleted in D relative to typical mare basalts from Apollo collections, and even lower than what have been measured for Apollo low-Ti basalt 12040 (Boyce et al., 2015; Treiman et al., 2016) and Kalahari 009 (Tartese et al., 2014). Indeed, if our inference is correct of a mare heritage for apatite in NWA 10989, data presented here would represent the lowest δD ever recorded in a mare basalt sample (i.e. ∼−400‰). Our work also shows that to infer the origin of lunar breccias, and the multiple reservoirs of volatiles that their individual components may have sampled, is not trivial. A combined approach based on H, Cl and age data on apatite is preferable, especially for apatites lacking a petrologic context.

Apatites #1 and #10 display signatures typical of mare basalts but their crystallization ages at ∼4–4.2 Ga makes them some of the oldest examples of volcanic products on the Moon (Terada et al., 2007; Snape et al., 2018). The rest of the apatites seem to display signatures more akin to KREEP-rich basalts rather than Mg or alkali-suite as the chlorine isotopes are much less fractionated than is the case for typical highlands samples, as well as the younger ages of these apatites (i.e. 3.3–3.9). However, no obvious KREEP-rich basaltic component has been found in NWA 10989. As a result, it seems likely that NWA 10989 has sampled a mare basalt reservoir that has not been identified for existing lunar samples.

4.2.3. Implication of the δD-δ^{37}Cl systematics in NWA 10989 phosphates

From combined hydrogen and chlorine isotopic studies on apatites from Apollo samples, three main reservoirs can be defined (cf. Fig. 11). For δD, Mg-and alkali suites range from +200 to −400‰ (Barnes et al., 2014), while their chlorine isotopic ratios are between +25 and +36‰ (Treiman et al., 2014; Barnes et al., 2016). KREEP-rich basalts cover a large range of both δD and δ^{37}Cl, respectively from −700 to +900‰ (Robinson et al., 2016) and from +14 to +40‰ (Sharp et al., 2010; Tartese et al., 2014; Barnes et al., 2016; Potts et al., 2018). Finally, Apollo mare basalts δD are typically higher than +500‰ (Tartèse et al., 2013; Barnes et al., 2013), while their δ^{37}Cl range from −4 to +18‰ (Sharp et al., 2010, Boyce et al., 2015, Barnes et al., 2016). However, basaltic lunar meteorite Kal 009 (Tartese et al., 2014) and Apollo sample 12040 (Boyce et al., 2015; Treiman et al., 2016) do not all plot in the "typical" Apollo mare basalt δD-δ^{37}Cl field and expand the range of δD for mare basalt, as they seem to record a D-depleted volatile reservoirs compared to other Apollo mare basalt samples. Kal 009 and Apollo 12040 D-poor reservoirs has to be distinct, as they are compositionally distinct (also notable is a fact that their crystallization ages differ by 1 Ga (Terada et al., 2017; Nyquist, 1977). NWA 10989 apatites also record a distinct mare basalt volatile reservoir, attesting that the Moon retains multiple volatile reservoirs (Robinson and Taylor, 2014; Boyce et al., 2018).

To account for the differences in these low δD signatures in some mare basalts compared to typical mare basalt δD signature, several hypotheses have been put forward. Elevated δD in lunar basaltic apatites have been argued to have resulted from magma degassing (Füri et al., 2014; Tartèse et al., 2014). On the other hand, assimilation of regolith containing solar wind H has been argued as a possibility to account for D-depleted signatures in mare basalts (Treiman et al., 2016).

4.3. Possible source regions of NWA 10989

The lunar breccia NWA 10989 is a lunar meteorite of intermediate-iron bulk composition composed of two distinct compositional sources – a magnesian highlands reservoir, mostly similar to Apollo FAN material, although more mafic, and a mixture of mare basalt reservoirs, one being similar to VLT basalts. As implied by its binary nature, NWA 10989 probably originated like other felsdpathic-mare breccias of intermediate-iron concentration from a region of the Moon where mare basalt has mixed with felsdpathic highland terrane (Korotev et al., 2009; Jolliff et al., 2000). Mare-highland boundaries do exist on the lunar nearside, potentially close to the Luna 24 or Apollo 17 landing sites where VLT basalts and FAN materials, similar to Apollo 16 materials, have been found. However, in NWA 10989, there is no substantial lithological evidence for KREEP-rich basalt material, despite 'Apollo Model' (Korotev et al., 2009) mass balance suggesting up to 3% KREEP, with 45% mare material and 52% feldspathic material. Indeed, all Apollo breccias consisting mainly of anorthositic material and basalt also contain a small KREEP component. The 'Apollo model' does not distinguish between mare basalts and mafic lithologies which may occur within highlands rocks. As such, in NWA 10989, the incompatible elements may be supplied by this mafic non-mare component (cf. Fig. 9), supported by the presence of ultramafic cumulate clasts; component which doesn't exist in the Apollo samples. As a result, we infer that NWA 10989 was derived from a mare–highland boundary region distant from the Procellarum KREEP Terrane on the Moon, similar to other binary brecciated anorthositic and mare-basalt breccias (Korotev et al., 2009).

Hydrogen and chlorine isotopic compositions of NWA 10989 apatites show a strong resemblance with the KREEP-rich breccia NW4472 (cf. Fig. 11). However, as stated previously, NWA 10989 does not contain any significant KREEP-rich basaltic material. Combined analyses of δD-δ^{37}Cl with age dating of apatites highlight two groups of apatites: one group which sampled a typical mare basalt-type source (i.e. $\delta D > +400‰$, $\delta^{37}Cl \sim 16‰$), while the other group sampled an unusual basaltic reservoir, with δD values as low as $-433 \pm 88‰$, similar to the older Mg-suite rocks from Apollo collections, but with chlorine isotope signature more akin to younger mare basalts. This evidence strongly argues for the presence of material in this breccia, which is either not yet identified in the Apollo collections or more likely represents an area of the Moon not sampled by the Apollo missions. As a result, a more probable source location for this breccia would be on a maria–highlands boundary on the lunar farside.

5. CONCLUSION

NWA 10989 is a lunar meteorite of intermediate-iron bulk composition with a mixture of ~40% mare basaltic material and ~60% feldspathic material. This meteorite does not contain any significant KREEP component which is in contradiction with estimation of a KREEP component based on the canonical 'Apollo Model', suggesting that this model may not be universally applicable to all lunar breccias. Based on hydrogen and chlorine isotopes, as well as age dating of apatite grains, NWA 10989 appears to have sampled at least two distinct mare basalt reservoirs on the Moon. Some apatites come from an ancient cryptomare reservoir, while the other apatites come from a D-depleted mare basalt reservoir relative to the source regions of typical mare basalts from Apollo collections, which has not been yet identified in lunar sample collection. These new data on lunar volatiles strongly favour the hypothesis that multiple volatile reservoirs are present on the Moon. NWA 10989 is thus an important lunar breccia, which most probably sampled a region different from any of the Apollo landing sites, possibly near a mare-feldspathic boundary on the farside of the Moon.

ACKNOWLEDGEMENTS

We dedicate this manuscript to the memory of Prof Larry Taylor who introduced one of the authors (MA) to the fascinating world of lunar sample science and provided many years of mentoring. We thank four anonymous reviewers, as well as Dr. James Day for his editorial handling, all of which greatly improved the quality of the manuscript. We also thank Graham Ensor for providing us with the sample of this lunar meteorite. MA and IAF acknowledge funding from Science and Technology Facilities Council (STFC) grants (#ST/I001964/1, #ST/L000776/1 and ST/P000657/1). All the authors acknowledge UKRI funding.

APPENDIX A. SUPPLEMENTARY MATERIAL

Supplementary data to this article can be found online at https://doi.org/10.1016/j.gca.2019.07.045.

REFERENCES

Anand M., Taylor L. A., Neal C. R., Snyder G. A., Patchen A., Sano Y. and Terada K. (2003a) Petrogenesis of lunar meteorite EET 96008. *Geochim. Cosmochim. Acta* **67**, 3499–3518.

Anand M., Taylor L. A., Misra K. C., Demidova S. I. and Nazarov M. A. (2003b) KREEPy lunar meteorite Dhofar 287A: a new lunar mare basalt. *Meteorit. Planet. Sci.* **38**, 485–499.

Anand M., Taylor L. A., Floss C., Neal C. R., Terada K. and Tanikawa S. (2006) Petrology and geochemistry of LaPaz Icefield 02205: a new unique low-Ti mare-basalt meteorite. *Geochim. Cosmochim. Acta* **70**, 246–264.

Anders E. and Grevesse N. (1989) Abundances of the elements: meteoritic and solar. *Geochim. Cosmochim. Acta* **53**, 197–214.

Arai T., Takeda H. and Warren P. H. (1996) Four lunar mare meteorites: crystallization trends of pyroxenes and spinels. *Meteorit. Planet. Sci.* **31**, 877–892.

Arai T. and Warren P. H. (1999) Lunar meteorite Queen Alexandra Range 94281: glass compositions and other evidence for launch pairing with Yamato 793274. *Meteorit. Planet. Sci.* **34**, 209–234.

Arai T., Hawke B. R., Giguere A., Misawa K., Miyamoto M. and Kojima H. (2010) Antarctic lunar meteorites Yamato-793169, Asuka-881757, MIL 05035, and MET 01210 (YAMM): Launch pairing and possible cryptomare origin. *Geochim. Cosmochim. Acta* **74**, 2231–2248.

Ashcroft H.O., Anand M., Korotev R.L., Greenwood R.C., Franchi I.A. and Strekopytov S. (2017) NWA 10989 – a new lunar meteorite with equal proportions of felsdpathic and VLT material. Lunar Planet. Sci. XLVIII. Lunar Planet. Inst., Houston. #1481(abstr.).

Barnes J. J., Franchi I. A., Anand M., Tartèse R., Starkey N. A., Koike M., Sano Y. and Russell S. S. (2013) Accurate and precise measurements of the D/H ratio and hydroxyl content in lunar apatites using NanoSIMS. *Chem. Geol.* **337–338**, 48–55.

Barnes J. J., Tartèse R., Anand M., McCubbin F. M., Franchi I. A., Starkey N. A. and Russell S. S. (2014) The origin of water in the primitive Moon as revealed by the lunar highlands samples. *Earth Planet. Sci. Lett.* **390**, 244–252.

Barnes J. J., Tartèse R., Anand M., McCubbin F. M., Neale C. R. and Franchi I. A. (2016) Early degassing of lunar urKREEP by crust-breaching impact(s). *Earth Planet. Sci. Lett.* **447**, 84–94.

Barnes J. J., Franchi I. A., McCubbin F. M. and Anand M. (2019) Multiple reservoirs of volatiles in the Moon revealed by the isotopic composition of chlorine in lunar basalts. *Geochim. Cosmochim. Acta* **266**, 144–162.

Bence A. E. and Papile J. J. (1972) Pyroxenes as recorders of lunar basalt petrogenesis: Chemical trends due to crystal-liquid interaction. *Proc. Lunar Sci. Conf.* **1**, 431–469.

Bouvier A., Gattacceca J., Grossman J. and Metzler K. (2017) The Meteoritical Bulletin No. 105. *Meteorit. Planet. Sci.* **52, 11**, 2411.

Boyce J. W., Treiman A. H., Guan Y., Ma C., Eiler J. M., Gross J., Greenwood J. P. and Stolper E. M. (2015) The chlorine isotope fingerprint of the lunar magma ocean. *Sci. Adv.* **1** e1500380.

Boyce J. W., Kanee S. A., McCubbin F. M., Barnes J. J., Bricker H. and Treiman A. H. (2018) Early loss, fractionation, and redistribution of chlorine in the Moon as revealed by the low-Ti lunar mare basalt suite. *Earth Planet. Sci. Lett.* **500**, 205–214.

Cahill J. T., Floss C., Anand M., Taylor L. A., Nazarov M. A. and Cohen B. A. (2004) Petrogenesis of lunar highlands meteorites: Dhofar 025, Dhofar 081, Dar al Gani 262, and Dar al Gani 400. *Meteorit. Planet. Sci.* **39**, 503–529.

Calzada-Diaz A., Joy K. H., Crawford I. A. and Strekopytov S. (2017) The petrology, geochemistry, and age of lunar regolith breccias Miller Range 090036 and 090070: insights into the crustal history of the Moon. *Meteorit. Planet. Sci.* **52**, 3–23.

Chao E. C. T., Mikin J. A. and Thompson C. L. (1976) The petrology of 77215, a noritic impact ejecta breccia. *Abstr. Lunar Planet. Sci. Conf.* **7**, 129.

Collareta A., D'Orazio M., Gemelli M., Pack A. and Folco L. (2016) High crustal diversity preserved in the lunar meteorite Mount DeWitt 12007 (Victoria Land, Antartica). *Meteorit. Planet. Sci.* **51**, 351–371.

Demidova S. I., Nazarov M. A., Lorenz C. A., Kurat G., Brandstatter F. and Ntaflos Th. (2007) Chemical composition of lunar meteorites and the lunar crust. *Petrology* **15**, 386–407.

Day J. M. D., Floss C., Taylor L. A., Anand M. and Patchen A. D. (2006) Evolved mare basalt magmatism, high Mg/Fe feldspathic crust, chondritic impactors, and the petrogenesis of Antarctic lunar breccia meteorites Meteorite Hills 01210 and Pecora Escarpment 02007. *Geochim. Cosmochim. Acta* **70**, 5957–5989.

Elardo S. M., Shearer C. K., Fagan A. L., Borg L. E., Gaffney A. M., Burger P. V., Neal C. R., Fernandes V. A. and McCubbin F. M. (2014) The origin of young mare basalts inferred from lunar meteorites Northwest Africa 4734, 032, and LaPaz Icefield 02205. *Meteorit. Planet. Sci.* **49**, 261–291.

Füri E., Deloule E., Gurenko A. and Marty B. (2014) New evidence for chondritic lunar water from combined D/H and noble gas analyses of single Apollo 17 volcanic glasses. *Icarus* **229**, 109–120.

Greenwood J. P., Itoh S., Sakamoto N., Warren P., Taylor L. 9. and Yurimoto H. (2011) Hydrogen isotope ratios in lunar rocks indicate delivery of cometary water to the Moon. *Nat. Geosci.* **4**, 79–82.

Greenwood R. C., Burbine T. H., Miller M. F. and Franchi I. A. (2017) Melting and differentiation of early-formed asteroids: the perspective from high precision oxygen isotope studies. *Chem. Erde* **77**, 1–43.

Gross J., Treiman A. H. and Mercer C. N. (2014) Lunar feldspathic meteorites: constraints on the geology of the lunar highlands, and the origin of the lunar crust. *Earth Planet. Sci. Lett.* **388**, 318–328.

Grove T. L. (1982) Use of exsolution lamellae in lunar clinopyroxenes as cooling rate speedometers: an experimental calibration. *Am. Mineral.* **67**, 251–268.

Hallis L. J., Anand M., Greenwood R. C., Miller M. F., Franchi I. A. and Russell S. S. (2010) The oxygen isotope composition, petrology and geochemistry of mare basalts: evidence for large-scale compositional variation in the lunar mantle. *Geochim. Cosmochim. Acta* **74**, 6885–6899.

Herwartz D., Pack A., Friedrichs B. and Bischoff A. (2014) Identification of the giant impactor Theia in lunar rocks. *Science* **344**, 1146–1150.

James O. B., Lindstron M. M., and Flohr M. K. (1989). Ferroan anorthosite from lunar breccia 64435: Implications for the origin and history of lunar ferroan anorthosites. In Proceedings, 19th Lunar and Planetary Science Conference, Houston, Texas, March 14–18, 1988, Cambridge University Press, Cambridge, pp. 219–243.

Jolliff B. L., Gillis J. J., Haskin A., Korotev R. L. and Wieczorek M. A. (2000) Major lunar crustal terranes: surface expressions and crust-mantle origins. *J. Geophys. Res.* **105**, 1497–4216.

Jolliff B. L., Korotev R. L. and Rockow K. M. (1998) Geochemistry and petrology of lunar meteorite Queen Alexandra Range 94281, a mixed mare and highland regolith breccia, with special emphasis on very-low-titanium mafic components. *Meteorit. Planet. Sci.* **33**, 581–601.

Joy K. H., Crawford I. A., Russell S. S. and Kearsley A. T. (2010) Lunar meteorite regolith breccias: an in situ study of impact met composition using LA-ICP-MS with implications for the composition of the lunar crust. *Meteorit. Planet. Sci.* **45**, 917–946.

Joy K. H., Burgess R., Hinton R., Fernandes V. A., Crawford I. A., Kearsley A. T. and Irving A. J. (2011) EIMF Petrogenesis and chronology of lunar meteorite Northwest Africa 4472: a KREEPy regolith breccia from the Moon. *Geochim. Cosmochim. Acta* **75**, 2420–2452.

Karner J., Papike J. J. and Shearer C. K. (2003) Olivine from planetary basalts: chemical signatures that indicate planetary parentage and those that record igneous setting and process. *Am. Mineral.* **88**, 806–816.

Karner J., Papike J. J. and Shearer C. K. (2006) Comparative planetary mineralogy: pyroxene major- and minor-element

chemistry and partitioning of vanadium between pyroxene and melt in planetary basalts. *Am. Mineral.* **91**, 1574–1582.

Korotev R. L. (1987) The nature of the meteoritic components of Apollo 16 soil, as inferred from correlations of iron, cobalt, iridium, and gold with nickel. *Proc. Lunar Planet. Sci. Conf.* **17th**, E447–E461.

Korotev R. L., Jolliff B. L. and Rockow K. M. (1996) Lunar meteorite Queen Alexandra Range 93069 and the iron concentration of the lunar highlands surface. *Meteorit. Planet. Sci.* **31**, 909–924.

Korotev R. L., Jolliff B. L., Zeigler R. A. and Haskin L. A. (2003) Compositional constraints on the launch pairing of three brecciated lunar meteorites of basaltic composition. *Antarctic Meteorite Research* **16**, 152–175.

Korotev R. L. (2005) Lunar geochemistry as told by lunar meteorites. *Chem. Erde* **65**, 297–346.

Korotev R.L. and Irving A. J. (2005) Compositions of three lunar meteorite: Meteorite Hills 01210, Northeast Africa 001, and Northwest Africa 3136. Lunar Planet. Sci. XXXVI, Lunar Planet. Inst., Houston. #1220(abstr.).

Korotev R. L., Zeigler R. A. and Jolliff B. L. (2006) Feldspathic lunar meteorites Pecora Escarpment 02007 and Dhofar 489: contamination of the surface of the lunar highlands by post-basin impacts. *Geochim. Cosmochim. Acta* **70**, 5935–5956.

Korotev R. L., Zeigler R. A., Jolliff B. L., Irving A. J. and Bunch T. E. (2009) Compositional and lithological diversity among brecciated lunar meteorites of intermediate iron concentration. *Meteorit. Planet. Sci.* **44**, 1287–1322.

Korotev R.L. and Zeigler R.A. (2014) ANSMET meteorites from the Moon. In Thirty-five Seasons of U.S. Antarctic Meteorites (1976-2010): A Pictorial Guide to the Collection (eds. K. Righter, R.P. Harvey, C.M. Corrigan and T.C. McCoy). Wiley, Washington, D.C., pp. 101–130.

Li Q.-L., Li X.-H., Wu F.-Y., Yin Q.-Z., Ye H.-M., Liu Y., Tang G.-Q. and Zhang C.-L. (2012) In-situ SIMS U-Pb dating of phanerozoic apatite with low U and high common Pb. *Gondwana Res.* **21**, 745–786.

Lorenzetti S., Busemann H. and Eugster O. (2005) Regolith history of lunar meteorites. *Meteorit. Planet. Sci.* **40**, 315–327.

Ludwig K. R. (2012). Isoplot 3.75: A geochronological toolkit for Microsoft Excel, Berkeley Geochronology Center Spec. Publ. no. 5, Berkeley, California.

McCubbin F. M., Steele A., Hauri E. H., Nekvasil H., Yamashita S. and Hemley R. J. (2010) Nominally hydrous magmatism on the Moon. *Proc. Natl. Acad. Sci.* **107**, 11223–11228.

McCubbin F. M., Hauri E. H., Elardo S. M., Vander Kaaden K. E. and Wang J. (2012) Hydrous melting of the martian mantle produced both depleted and enriched shergottites. *Geology* **40**, 683–686.

McGee J. J. (1993) Lunar ferroan anorthosites: mineralogy, compositional variations, and petrogenesis. *J. Geophys. Res.* **98**, 9089–9105.

Meyer H. O. A., Hwang J. Y. and McCallister R. H. (1978). In *Luna 24: Mineral Chemistry of 90–150 Micron Clasts*. Pergamon Press, New York, pp. 2137–2147.

Miller M. F., Franchi I. A., Sexton A. S. and Pillinger C. T. (1999) High precision δ17O isotope measurements of oxygen from silicates and other oxides: method and applications. *Rapid Commun. Mass Spectrom.* **13**, 1211–1217.

Miller M. F., Franchi I. A., Thiemens M. H., Jackson T. L., Brack A., Kurat G. and Pillinger C. T. (2002) Mass-independent fractionation of oxygen isotopes during thermal decomposition of carbonates. *Proc. Natl. Acad. Sci.* **99**, 109888-10993.

Neal C. R. and Taylor L. A. (1992) Petrogenesis of mare basalts: a record of lunar volcanism. *Geochim. Cosmochim. Acta* **56**, 2177–2211.

Nielsen R. L. and Drake M. J. (1978) The case for at least three mare basalt magmas at the Luna 24 landing site. In *Mare Crisium: The View from Luna 24* (eds. R. B. Merrill and J. J. Papike), pp. 419–428.

Norman M. D. and Nemchin A. A. (2014) A 4.2 billion year old impact basin on the Moon: U-Pb dating of zirconolite and apatite in lunar melt rock 67955. *Earth Planet. Sci. Lett.* **388**, 387–398.

Nyquist L. E. (1977) Lunar Rb-Sr chronology. *Phys. Chem. Earth.* **10**, 103–142.

Papike J., Taylor L. and Simon S. (1991) Lunar minerals. In *Lunar Sourcebook: A User's Guide to the Moon* (eds. G. H. Heiken, D. T. Vaniman and B. M. French). Cambridge University Press, Cambridge, pp. 121–181.

Papike J. J., Ryder G., and Shearer C. K. (1998) Lunar samples. In Planetary Materials. Reviews in Mineralogy 36 (ed. J.J. Papike), Mineralogical Society of America, Washington, D.C., pp. 5-1 to 5-234.

Pillinger C.T., Greenwood R.C., Gibson J.M., Pillinger J.M., Gibson E.K. (2013) The Holbrook meteorite – 99 years out in the weather, Lunar Planet. Sci. XXVIII. Lunar Planet. Inst., Houston. #2883(abstr.).

Potts N., Barnes J. J., Tartese R., Franchi I. A. and Anand M. (2018) Chlorine isotopic compositions of apatite in Apollo 14 rocks: evidence for widespread vapor-phase metasomatism on the lunar nearside ~4 billion years ago. *Geochim. Cosmochim. Acta* **230**, 46–59.

Robinson K. L. and Taylor G. J. (2014) Heterogeneous distribution of water in the Moon. *Nature Geosci.* **7**, 401–408.

Robinson K. L., Barnes J. J., Nagashima K., Thomen A., Franchi I. A., Huss G. R., Anand M. and Taylor G. J. (2016) Water in evolved lunar rocks: evidence for multiple reservoirs. *Geochim. Cosmochim. Acta* **188**, 244–260.

Rubin A. E., Scott E. R. and Keil K. (1997) Shock metamorphism of enstatite chondrites. *Geochim. Cosmochim. Acta* **61**, 847–858.

Ruzicka A., Grossman J., Bouvier A., Herd C. D. K. and Agee C. B. (2015) The Meteoritical Bulletin No. 102. *Meteorit. Planet. Sci.* **50**, 1662.

Schoene B., Crowley J. L., Condon D. J., Schmitz M. D. and Bowring S. A. (2006) Reassessing the uranium decay constants for geochronology using ID-TIMS U-Pb data. *Geochim. Cosmochim. Acta* **70**, 426–445.

Sharp Z. D., Shearer C. K., McKeegan K. D., Barnes J. D. and Wang Y. Q. (2010) The chlorine isotope composition of the Moon and implications for an anhydrous mantle. *Science* **329**, 1050–1053.

Shearer C. K., Elardo S. M., Petro N. E., Borg L. E. and McCubbin F. M. (2015) Origin o the lunar highlands Mg-suite: An integrated petrology, geochemistry, chronology, and remote sensing perspective. *Am. Mineral.* **100**, 294–325.

Snape J. F., Curran N. M., Whitehouse M. J., Nemchin A. A., Joy K. H., Hopkinson T., Anand M., Bellucci J. J. and Kenny G. G. (2018) Ancient volcanism on the Moon: Insights from Pb isotopes in the MIL 13317 and Kalahari 009 lunar meteorites. *Earth Planet. Sci. Lett.* **502**, 84–95.

Spicuzza M. J., Day J. M. D., Taylor L. A. and Valley J. W. (2007) Oxygen isotope constraints on the origin and differentiation of the Moon. *Earth Planet. Sci. Lett.* **253**, 254–265.

Starkey N. A., Jackson C. R. M., Greenwood R. C., Parman S., Franchi I. A., Jackson M., Fitton J. G., Stuart F. M., Kurz M. and Larsen L. M. (2016) Triple oxygen isotopic composition of the high – $^{3}He/^{4}He$ mantle. *Geochim. Cosmochim. Acta* **176**, 227–238.

Stelzer T. H., Heide K., Bischoff A., Weber D., Schultz L., Happel M., Schron W., Neuper U., Micehl R., Clayton R. N., Mayeda

T., Bonani G., Haidas I., Ivy-Ochs S. and Suter M. () An interdisciplinary study of weathering effect in ordinary chondrites from Acfer region, Algeria. *Meteorit. Planet. Sci.* **34**, 787–794.

Stephant A., Garvie L. A. J., Mane P., Hervig R. and Wadhwa M. (2018) Terrestrial exposure of a fresh Martian meteorite causes rapid changes in hydrogen isotopes and water concentrations. *Sci. Rep.* **8**, 12385.

Tartèse R., Anand M., Barnes J. J., Starkey N. A., Franchi I. A. and Sano Y. (2013) The abundance, distribution, and isotopic composition of hydrogen in the Moon as revealed by basaltic lunar samples: implications for the volatile inventory of the Moon. *Geochim. Cosmochim. Acta* **122**, 58–74.

Tartèse R., Anand M., Joy K. H. and Franchi I. A. (2014) H and Cl isotope systematics of apatite in brecciated lunar meteorites Northwest Africa 4472, Northwest Africa 773, Sayh al Uhaymir 169, and Kalahari 009. *Meteorit. Planet. Sci.* **49**, 2266–2269.

Taylor G.J., Warren P.H., Ryder G., Delano J., Pieters C. and Lofgren G. Lunar Rocks. Lunar minerals, In: Heiken G.H., Vaniman D.T. and French B.M., (Eds.), Lunar Sourcebook: A User's Guide to the Moon, 1991, Cambridge University Press; Cambridge, 183-284.

Terada K., Anand M., Sokol A. K., Bischoff A. and Sano Y. (2007) Cryptomare magmatism 4.35 Gyr ago recorded in lunar meteorite Kalahari 009. *Nature* **450**, 849–853.

Treiman A. H., Boyce J. W., Gross J., Guan Y., Eiler J. M. and Stolper E. M. (2014) Phosphate-halogen metasomatism of lunar granulite 79215: impact-induced fractionation of volatiles and incompatible elements. *Am. Mineral.* **99**, 1860–1870.

Treiman A. H., Boyce J. W., Greenwood J. P., Eiler J. M., Gross J., Guan Y., Ma C. and Stopler E. M. (2016) D-poor hydrogen in lunar mare basalts assimilated from lunar regolith. *Am. Mineral.* **101**, 1596–1603.

Vaniman D. T. and Papike J. J. (1977) Very low Ti (VLT) basalts: a new mare rock type from the Apollo 17 drill core. Proceedings of the Lunar and Planetary Conference VIII , Houston, Texas, March 14-18, 1977, Pergamon Press, New York, pp. 1443–1471.

Warren P. H. (2012) Let's get real: Not even lunar rocks sample is big enough to be representative for every purpose. *Second Conference on the Lunar Highlands Crust.*, #9034(abstr.).

Warren P. H. and Wasson J. T. (1979) The origin of KREEP. *Rev. Geophys.* **17**, 73.

Warren P. H. and Kallemeyn G. W. (1991) Geochemical investigation of five lunar meteorites: implications for the composition, origin and evolution of the lunar crust. *Proceedings of the NIPR Symposium on Antarctic Meteorites* **4**, 91–117.

Wiechert U., Halliday A. N., Lee D. C., Snyder G. A., Taylor L. A. and Rumble D. (2001) Oxygen isotopes and the moon-forming giant impact. *Science* **294**, 345–348.

Young E. D., Kohl E. I., Warren P. H., Rubie D. C., Jacobson S. A. and Morbidelli A. (2016) Oxygen isotopic evidence for vigorous mixing during the Moon-forming giant impact. *Science* **351**, 493–496.

Zhou Q., Herd C. D. K., Yin Q.-Z., Li X.-H., Wu F.-Y., Li Q.-L., Liu Y., Tang G.-Q. and McCoy T. J. (2013) Geochronology of the Martian meteorite Zagami revealed by U-Pb ion probe dating of accessory minerals. *Earth Planet. Sci. Lett.* **374**, 156–163.

Associate editor: James M.D. Day